공학박사학위논문

Film-forming Mechanism of Sulfur-containing Additives on Graphite Negative Electrodes and Their Low-temperature Performances

리튬 이온 전지용 흑연 음극에서 황을 포함하는 첨가물의 표면 필름 형성 과정 및 저온 성능

2016년 2월

서울대학교 대학원

화학생물공학부

정 선 형

ABSTRACT

Film-forming Mechanism of Sulfur-containing Additives on Graphite Negative Electrodes and Their Low-temperature Performances

Sunhyung Jurng

Department of Chemical and Biological Engineering

Seoul National University

Lithium ion batteries (LIB) have been applied as a major power source for portable electric devices due to high energy density and long life cycles. Lately, they are the most promising candidate for hybrid electric vehicles (HEVs) and pure electric vehicles (EVs). There are, however, a series of technical barriers in LIB must first be overcome, one of which is the drastic decrease in various aspects of performance in cold condition. It is well known that graphite, which represents the preferred negative electrode for LIB, delivers poor electrochemical performance at low-temperatures.

The performance indicators of graphite electrode, like irreversible capacity, rate capability, cycleability and safety are highly dependent on characteristics of solid electrolyte interphase (SEI), which inevitably passivates the surface of graphite. Film-forming additives can be used as one way to optimize the chemical composition and physio-chemical properties of SEI, leading to improved

performances of LIB. Two additive types are studied in this thesis, elemental sulfur as an electrode additive and allyl sulfide as an electrolyte additive. Both additives improve the low-temperature performance of the graphite electrode. Of the two, the latter type has an advantage of stability in cell operation.

In the first half of the thesis, the film-forming mechanism and the low-temperature performance of elemental sulfur additive are studied. In the first lithiation step, the elemental sulfur is electrochemically reduced to be lithium polysulfide (Li_2S_8), which is soluble in the working solvent (carbonate-based). Organic thiocarbonates are generated by the chemical reaction between the lithium polysulfide and carbonate solvents. The as-generated thiocarbonates are then electrochemically decomposed to form the sulfur-containing surface film. The sulfur-added graphite shows better reversible capacity at low-temperature, also, Li plating is suppressed. The superior low-temperature performance of the sulfur-added graphite is thus attributed to the presence of sulfur-enriched surface film with less inorganic species, which seems to facilitate the charge transfer reaction between the graphite and lithium.

Secondly, allyl sulfide (AS) additive is examined along the same lines. In 12 hr rest period before cycle, allyl sulfide additive is oxidized spontaneously and forms film on the surface of graphite. This pre-formed film is reduced and develops sulfur and carbon rich inner film onto the graphite. The low-temperature performance of the AS-added graphite is also superior to the control one, in reversible capacity and prevention of Li plating. This is attributed to the chemical aspects of surface film, like in case of elemental sulfur additive. Since AS additive

does not involve side reactions during film formation, it has an advantage of stability in cell operation over elemental sulfur.

Keywords: Low-temperature performance, Graphite negative electrode, Sulfur, Allyl sulfide, Lithium ion batteries

Student Number: 2009-23957

CONTENTS

LIST OF FIGURES

Fig. 39. Schematic illustration for the film-forming process of allyl sulfide additive.

LIST OF TABLES

1. INTRODUCTION

Increases in oil price and greenhouse gas emission have increased the need for hybrid electric vehicles (HEV) and pure electric vehicles (EV). Lithium ion batteries (LIB) are the most promising candidate for these applications due to their high energy and power density relative to other power sources. For application in electrified vehicles, a series of technical barriers in LIB must first be overcome, one of which is the drastic decrease in various aspects of performance at low temperatures [1]. It has been reported that a commercial 18650 LIB delivers an energy density of only 5% at -40^{o}C compared to the value at 20^{o}C [2]. The capacity decrease is momentary and the degree of decline is related to the chemistry of battery. According to the U.S. Department of Energy, LIB in power-assisted HEVs should function at -30^{o}C and survive at -46^{o}C [3].

It is well known that graphite, which represents the preferred negative electrode for LIB, delivers poor electrochemical performances below -20^{o}C [4-6]. Despite its favorable properties such as a theoretical specific capacity of 372 mAh g^{-1} and low working potential close to that of lithium, this reduced ability of graphite at low-temperature limits its application to electrified vehicles. The inferior performance of graphite at low temperatures has been attributed to several factors; (i) the viscosity of electrolytes are increased and consequently Li^{+} conductivity is declined, (ii) Li^{+} ion mobility is decreased in the surface films called solid electrolyte interphase (SEI), (iii) charge transfer resistance is increased at the electrode/electrolyte interface, and (iv) reduced solid-state Li^{+} diffusivity

within the graphite structure. Several approaches have been pursued to overcome these limitations [4,6-8], one of which is the use of propylene carbonate (PC) instead of ethylene carbonate (EC) as the solvent. With PC, the conductivity problem can be somewhat overcome because the freezing point is lower for PC. Unfortunately, however, PC is not compatible with graphite electrode because of exfoliation problem [9].

Electrolyte decomposition and film deposition are unavoidable in graphite negative electrodes because their working voltage is beyond the thermodynamic stability window of common organic electrolytes. The SEI film, which is formed at electrode/electrolyte interface, passivates the graphite surface and prevents additional electrolyte decomposition. The cell performance indicators like irreversible capacity, rate capability, cycleability and safety are highly dependent on the characteristics of SEI [10-13]. Moreover, the low-temperature performance is influenced by the features of SEI. Film-forming additives can be used as one way to optimize the chemical composition and physio-chemical properties of SEI, leading to improved performances of LIB.

To modify the properties of SEI for improving performance in low-temperature, sulfur-containing additives were applied to a Li/graphite cell. The SEI film consisting of sulfur compounds was expected to be favorable in cold environment in two aspects. First, sulfide based glassy solid electrolytes, such as $Li_2S–P_2S_5$ system shows high conductivity over 10^{-4} S cm^{-1} at room temperature [14-18]. Second, the addition of sulfur bond (sulfur bridge) between polymer chains improves the elasticity of polymer structure, and prevents turning brittle at

low-temperature. In the earlier reports, sulfur-based compounds including SO_2 [19], CS_2 [20], polysulfide [21,22], and sulfites [23,24] were used as additives in LIB. It has been reported that the SEI derived from polysulfide exhibits a reduced resistance related to the charge transfer reaction [21], however, the detailed analysis has not been reported yet.

Two additive types were studied in this thesis, elemental sulfur as an electrode additive and allyl sulfide as an electrolyte additive. The purpose of this thesis was to understand the film-forming mechanism of the two sulfur-containing additives during pre-cycling, and the relation between the chemical aspects of SEI and the low-temperature performance of graphite electrode. To trace the film-forming pathway from additive to sulfur-enriched film, X-ray photoelectron spectroscopy (XPS) and electrochemical analysis are employed. The low-temperature capacity and occurrence of Li plating were compared for the additive-added and additive-free graphite electrode, and impedance measurement was made to account for the difference in electrode polarization between two electrodes.

2. BACKGROUND

2.1. Electrochemical Cells

Electrochemistry is the study of the conversion of electrical and chemical energy system. The electrochemical conversion can be divided into two types of reactions; the loss of electrons (oxidation), and the gain of electrons (reduction).

$$Fe^{2+} \rightarrow Fe^{3+} + e \text{ (oxidation)}$$

$$Cu^{2+} + 2e \rightarrow Cu^{0} \text{ (reduction)}$$

An electrochemical cell makes use of an above redox reaction to produce an electric energy. Basically, an electrochemical cell consists of two electrodes, the anode and the cathode, separated by an electrolyte-permeable separator with a liquid electrolyte. In the electrochemical cell system, the ionic component of each chemical reaction moves between two electrodes while the electronic component traverses an external circuit to form a “closed loop” (Fig. 1). A cell should have large-area electrodes kept apart by a thin electrolyte, since the ionic mobility in the liquid electrolyte is much smaller than the electronic conductivity in a metal.

In an electrochemical cell, the definition of electrical potential is the energy required to move a unit positive charge from an infinite distance to a specific phase against an electric field. The energy of electron is in inverse proportion to an electrical potential. The standard cell potential, often called the electromotive force

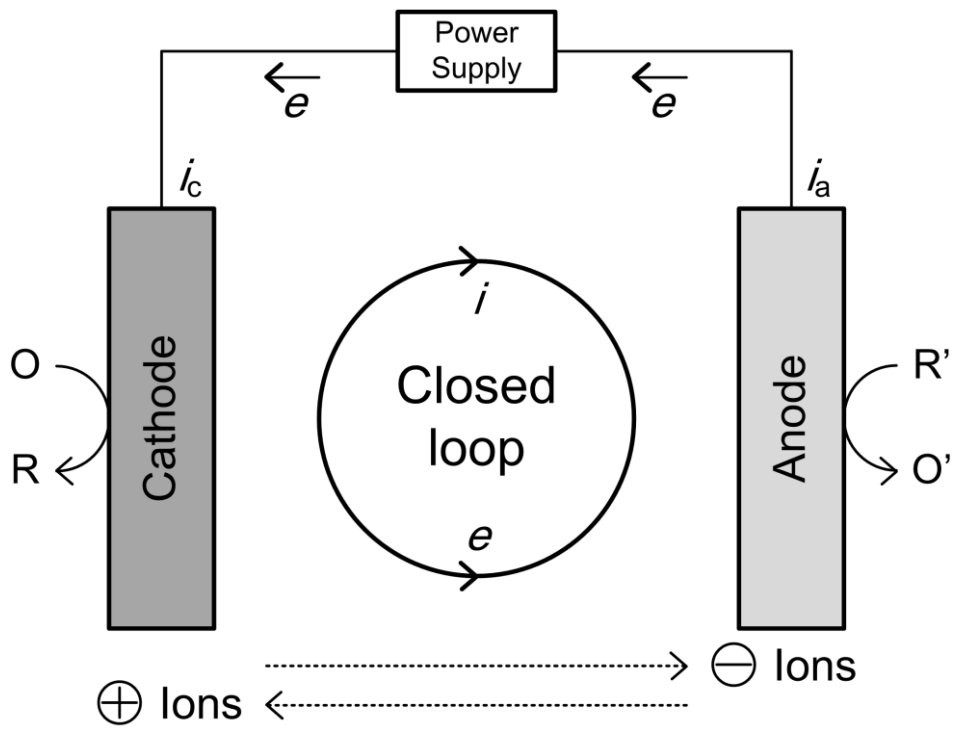

Fig. 1. The closed loop system in the electrochemical cell consisting of two electrodes, electrolyte, and power supply.

(emf) can be calculated from the change in Gibbs free energy:

$$\Delta G^0 = -nFE^0$$

- ΔG^0 is the Gibbs free energy change for a system under standard conditions (1 atm, 298 K)
- F is the Faraday constant, $9.6485 \times 10^4\ C\ equiv^{-1}$
- E^0 is the standard cell potential (V)

Electrochemical reactions hardly take place under standard conditions, because concentration of species involved in the electrochemical reaction vary during the process of reactions. The Nernst equation can be used for electrochemical cells under non-standard conditions.

$$E_{eq} = E^0 + \frac{RT}{nF}\ln\frac{\alpha_A^a \cdot \alpha_B^b \cdots}{\alpha_C^c \cdot \alpha_D^d \cdots}$$

- α_x is an activity of substance x
- R is the gas constant, $8.314\ J\ mol^{-1}K^{-1}$
- T is an absolute temperature (K)

2.2. Lithium Ion Batteries

2.2.1. Principles of Operation

The lithium ion battery is a type of rechargeable battery in which lithium ions are shuttled from the anode (negative electrode) to the cathode (positive electrode) during discharge, and in reverse when charging. This principle is known as "rocking chair" system (Fig. 2). Both electrodes have sites for the lithium ion storage and allow lithium ions to move in and out of their structures. The following equations show the electrochemical reaction occurred in a typical graphite/$LiCoO_2$ lithium ion battery.

$$Li_{1-x}CoO_2 + xLi^+ + xe \leftrightarrows LiCoO_2 \qquad \text{(Positive electrode)}$$

$$Li_xC_6 \leftrightarrows xLi^+ + xe + C_6 \qquad \text{(Negative electrode)}$$

2.2.2. History and Development

M. S. Whittingham proposed the first lithium batteries in the 1970s, which consist of titanium (IV) sulfide and lithium metal [25]. Because of their high price and sensitivity to air, these batteries were not commercialized. Metallic lithium electrodes inevitably have safety issues, since lithium is a highly reactive element; pure lithium reacts violently when placed in contact with water and air. For this reason, research moved to develop another system using lithium compounds which have storage sites for lithium ions.

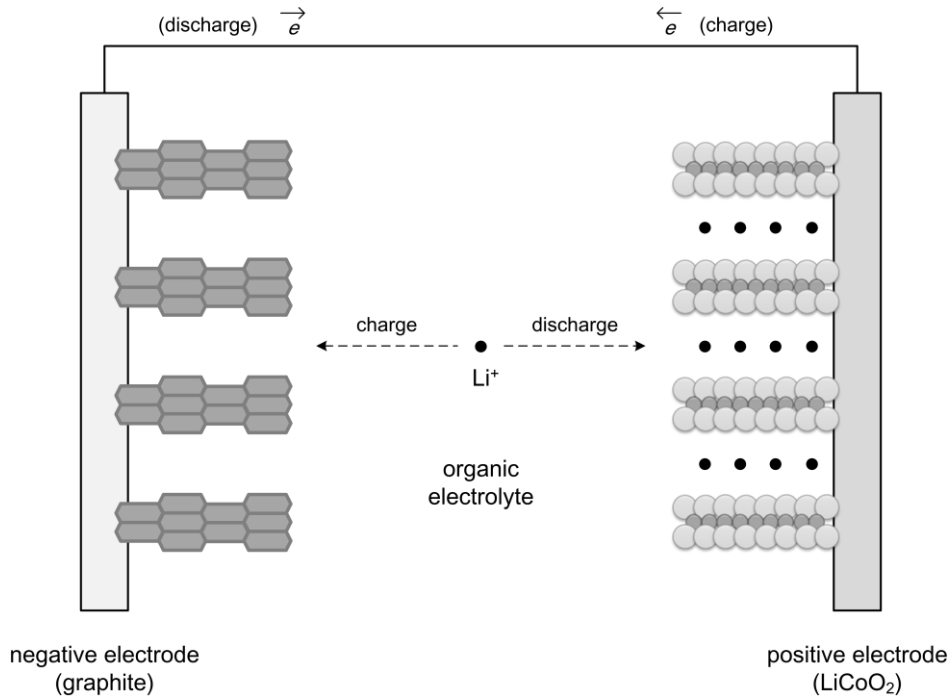

Fig. 2. A schematic illustration of the operating principles of a typical graphite/$LiCoO_2$ lithium ion battery.

In the 1970s, J. O. Besenhard reported two important phenomena, reversible ion intercalation in graphite [26,27] and cathodic oxides [28,29], and also their application in lithium ion batteries [30,31]. The most common electrode materials now in use, $LiCoO_2$ and graphite, were invented in the early 1980s. J. Goodenough demonstrated a rechargeable cell using $LiCoO_2$ [32]. $LiCoO_2$ is a stable material which can supply lithium ions, thus this positive electrode has no occasion to be combined with lithium metal negative electrode. In the same year, 1980, R. Yazami reported the reversible intercalation of lithium ion in graphite structure, using a solid electrolyte system [33]. SONY released the first commercial lithium ion batteries in 1991, by adopting $LiCoO_2$ and carbon electrodes.

2.2.3. Negative Electrode Materials

2.2.3.1. Lithium Metal

Lithium is the third lightest element and also has the highest possibility of being oxidized of all known elements; the standard electrode potential of this material is -3.04 V *vs.* SHE (standard hydrogen electrode). Thus, lithium batteries present the best prospects for achieving a high energy and high power energy storage system to satisfy the requirements for an electrified vehicles. In early days, lithium metal has been considered the “ideal” negative electrode because of its high capacity without an inactive host material. Metallic lithium provides a theoretical capacity of 3860 mAh g^{-1}, low density (0.59 g cm^{-3}), and the lowest theoretical electrode potential.

In spite of these advantages, lithium metal was not commercialized due to its stability issues coming from electrode/electrolyte interactions. Organic electrolytes react to form various products, including $ROCO_2Li$, Li_2CO_3, and ROLi species. The salt anion and its related products, PF_6^-, HF, and PF_5, also react on the lithium surface. These various reactions form a surface film on lithium electrode which has a complicated chemistry [34,35]. The multilayer surface film on lithium is non-uniform, thus induces non-uniform current distribution of deposition/dissolution of lithium [36,37]. Hence, the surface films formed on lithium tend to be easily cracked during a cell operation, leading to the formation of porous dendritic structures which can cause a loss in Coulombic efficiency and safety hazards; gas evolution and ignition of the electrolyte [38,39]. For these reasons, practical applications of lithium metal electrode have been prevented.

2.2.3.2. Carbonaceous Materials

Carbonaceous materials can be divided into two major allotropes; diamond (sp^3-carbon) and graphite (sp^2-carbon). From among these, graphite and sp^2-carbon based compounds, such as hard carbon, soft carbon, and carbon nanotube (CNT) are candidates for negative electrodes in lithium ion batteries.

Graphite, commercially available material as a negative electrode, is a layered compound consisting of hexagonal planes of sp^2-carbon atoms (grapheme sheets), which are arranged in the ABAB sequence along the c-axis. Lithium ions are stored between the graphitic interlayer, namely “intercalated”, and the theoretical capacity of graphite is 372 mAh g^{-1} (LiC_6). Crystalline graphite has two types of

characteristic surfaces, which are relative inactive basal plane (perpendicular to c-axis) and fairly active edge plane (parallel to c-axis). Reactions related with lithium ion occur mainly at the edge plane, under 0.3 V (*vs.* Li/Li^+), as low as lithium metal. The intercalation compound of lithium ion into graphite, a graphite intercalation compound (GIC), passes through several characteristic staged phases during lithiation. In this process, lithium ion is inserted into one interlayer gap by a periodic sequence [40]. R. Yazami reported that the lithium intercalation into graphite prevents the dendrite formation, while the rate of charge is restricted [33].

Other than graphite, two types of carbon are proposed as negative electrode materials. Soft carbon, called graphitized carbon, has an oriented structure where crystallites are arranged in the same direction, while hard carbon has disordered orientations. Under the heat treatment over 2500^oC, soft carbon can be graphitized, whereas hard carbon is hardly changed because of its disordered structure. The electrochemical performances depend strongly on the microstructure and morphology of these materials. The intercalation reaction of lithium rarely take place for soft and hard carbon, since crystallites consisting of graphitic layers are relatively small. These carbons store lithium ions mostly by adsorption or cluster formation [41,42].

2.2.3.3. Lithium Alloy-based Materials

Since graphite has a limited capacity and a potential safety hazard due to kinetic problem, lithium alloy-based materials (Si, Sn and Sb) have been addressed [43-45]. Among the lithium alloy elements, Group IV elements such as Si and Sn

are mainly focused owing to the high capacity lithium-rich binary alloys.

At elevated temperature, electrochemical reactions of lithium with Si yield intermetallic phases such as $Li_{12}Si_7$, Li_7Si_3, $Li_{13}Si_4$, and $Li_{22}Si_5$, which have distinctive plateaus [46]. At room-temperature, however, pure Si only can turn to be $Li_{15}Si_4$ phase, and the theoretical capacity is 3580 mAh g^{-1} [47]. Sn reacts with lithium to produce seven different Li-Sn binary phases: Li_2Sn_5, LiSn, Li_7Sn_3, Li_5Sn_2, $Li_{13}Sn_5$, Li_7Sn_2, and $Li_{22}Sn_5$ [48]. Based on $Li_{17}Sn_4$ alloy phase, each Sn atom can store 4.25 atoms of lithium with a working potential of about 0.5 V (*vs.* Li/Li^+) and the theoretical capacity is 960 mAh g^{-1}. Though Sn has a lower gravimetric capacity than Si, it is still an appealing candidate because of its volumetric capacity of about 2000 mAh cm^{-3}.

In spite of these merits, the intrinsic problem of large volume change has hindered the application of alloy-based materials. During lithiation/de-lithiation process, their volume expansion goes up to 400% [49]. Due to mechanical failure and electrical disconnection of the active material caused by the large volume change, alloy-based materials generally have a poor cycling ability [47]. This could be improved either by adopting a multi component complex, a thin-film fabrication, and an electrolyte additive [49,50].

2.2.4. Positive Electrode Materials

2.2.4.1. Layered Oxides

Since $LiCoO_2$ was demonstrated [32], transition metal oxides have been

extensively investigated as the positive electrode materials in lithium ion batteries. In the ideal structure of layered compounds ($LiMO_2$), the oxygen anions form a close-packed *fcc* lattice structure and the MO_2 slabs and lithium layers are stacked alternatively. The commercialized material, $LiCoO_2$, can only deliver about 140 mAh g^{-1} which is half of its theoretical capacity, since the structure converted into monoclinic form irreversibly when $x > 0.5$ in $Li_{1-x}CoO_2$ during de-lithiation process [51]. Over 4.3 V (correspond to $Li_{0.5}CoO_2$), oxygen evolution occur, leading to decrease of reversible capacity. In the elevated temperature this structural collapse can introduce safety issues [52].

2.2.4.2. Spinel Compounds

Spinel lithium manganese oxide ($LiMn_2O_4$), a candidate for an alternative to $LiCoO_2$, has many advantages including high rate performance and a competitive price. The oxygen framework of this material is the same as that of layered oxides. Lithium ions are located the tetrahedral sites in lithium layer sharing faces with the empty octahedral sites in the MO2 slaps. During de-lithiation process, two voltage plateaus appear around 4.0 V, indicating a two-step reaction. This material was found to have cell degradation problem, because of two reasons: (i) dissolution of Mn^{2+} through disproportionation of Mn^{3+} and (ii) Jahn-Teller distortion during cycle [53,54].

2.2.5. Electrolytes

2.2.5.1. Organic Solvents

Because lithium ion batteries are operated beyond the working potential of aqueous electrolytes, the current systems use mixtures of organic electrolytes including ethylene carbonate (EC), dimethyl, diethyl, and ethyl-methyl carbonates (DMC, DEC, EMC, respectively) as an electrolyte solvent [55]. These alkyl carbonates were adopted due to their reasonable stability in the electrochemical potential window of lithium ion batteries, high polarity (good conductivity), an acceptable temperature range, low toxicity, and safety features. EC is the most common electrolyte component, and a compulsory element for passivation of negative electrodes . The types and ratio of linear carbonates can be controlled depending on the purpose.

2.2.5.2. Lithium Salts

Lithium salts investigated in the lithium ion battery system are very limited compared to the electrode candidates as well as solvent combinations. While organic solvents are reasonably non-toxic and optimized for performance, the lithium conducting salts still have some hurdles to be overcome. The commercially available inorganic salts are $LiPF_6$, $LiBF_4$, $LiClO_4$, $LiAsF_6$, and $Li(CF_3SO_2)_2N$. Among these, $LiPF_6$ remains the only candidate to be used in commercial lithium ion batteries, so that replacing the salt will involve certain trade-offs.

2.2.6. Solid Electrolyte Interphase (SEI)

The solid electrolyte interphase (SEI) is a passivation film formed on the negative electrode in consequence of electrolyte reduction, mostly during the 1st cycle lithiation. The formation of SEI film on graphite electrodes is unavoidable because the working voltage is beyond the thermodynamic stability window of organic electrolytes. The SEI film passivates the graphite surface and affects the kinetics of lithiation/de-lithiation and thus the performance of the whole cell [56-58]: efficiency, rate capability, cyclability, safety, and low-temperature performances [59-61].

The composition and structure of the SEI have been studied for decades, but are not clear. Therefore it is very difficult to make a standard model of SEI. General contents of the SEI being reported are $(CH_2OCO_2Li)_2$, $ROCO_2Li$, Li_2CO_3, LiF, Li_2O, LiOH and also polycarbonates [10]. SEI is basically electrical insulator, while lithium ion can pass through the SEI layer. After SEI formation, thus, electrochemical reactions are prohibited at the electrode/electrolyte interface.

Film-forming additives can be used to modify the chemical and physical properties of SEI film, leading to better performances of lithium ion batteries [62]. The optimum amount of an additive in the electrolyte generally not exceed 5 % by weight or by volume, however, the improvement of performance is significant. Each additive performs one or more useful functions and improves the battery performance: SEI morphology modifier, positive electrode protector, salt stabilizer, safety protection agent, fire-retardant, lithium deposition improver, or Al corrosion inhibitor [63].

3. EXPERIMENTAL

3.1. Electrochemical Analysis

3.1.1. Electrode and Cell Preparation

3.1.1.1. Elemental Sulfur Additive for Electrode

We prepared composite graphite electrodes, which were fabricated by binding a graphite powder (Sodiff Co., Ltd., DAG 87), conducting agent (Super P), polyvinylidene fluoride (PVdF, polymeric binder) and sulfur powder (Aldrich) as an additive. Table 1 shows respectively the electrode composition of the sulfur-added graphite electrode and the sulfur-free one. The powders and PVdF were mechanically blended by stirring the mixture with N-methyl pyrrolidone (NMP) for 1 hr in a closed container using a magnetic stirrer, and then pasted onto a copper foil. The electrodes were dried for 12 hr in a vacuum and transferred to a glovebox (under Ar atmosphere). 2032-type two-electrode coin cells were assembled with Li foil (Cyprus Co., as a counter electrode) and a separator which is a trilayer of PP-PE-PP (polyethylene, polypropylene, Celgard). The electrolyte used was 1.3 *M* Li hexafluorophosphate ($LiPF_6$) dissolved in ethylene carbonate (EC), ethyl methyl carbonate (EMC) and diethyl carbonate (DEC) (3:2:5 in vol. ratio). As a reference, a coin cell using a graphite electrode without any sulfur additive (DAG87:super P:PVdF=90:5:5 in wt. ratio) was also fabricated. The morphology of graphite electrode is demonstrated in Fig. 3.

[wt.%]	Active material	Super-P	PVdF binder	Sulfur additive
Sulfur-free	90	5	5	-
Sulfur-added	89.5	5	5	0.5

Table 1. The electrode composition of the graphite electrode containing elemental sulfur additive and the reference one

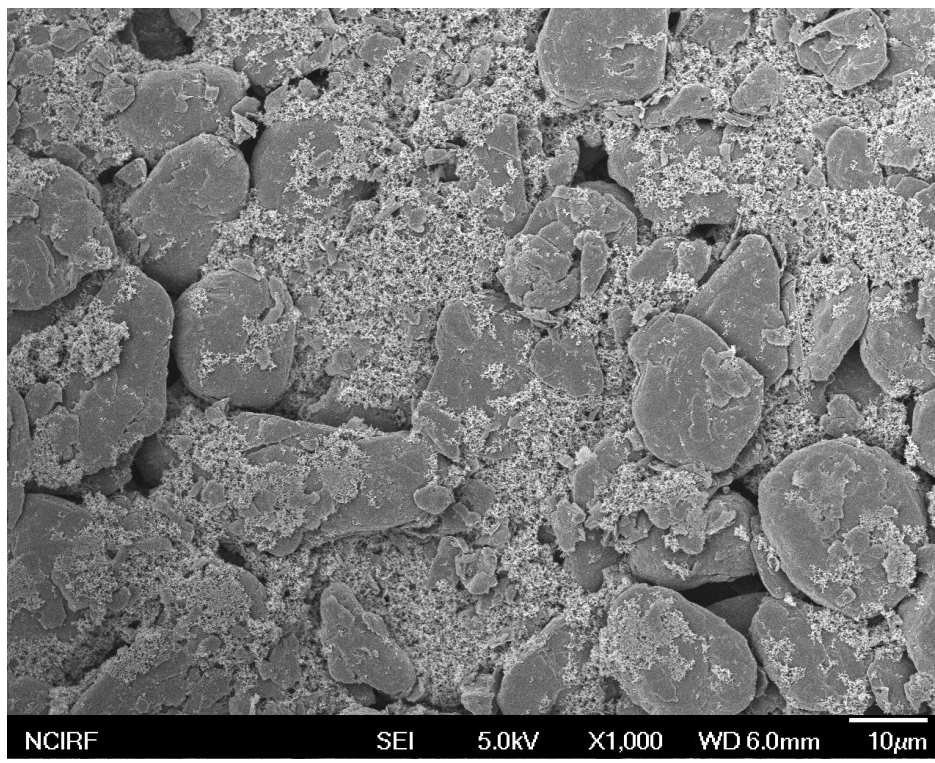

Fig. 3. FE-SEM image of the reference graphite electrode.

3.1.1.2. Allyl Sulfide Additive for Electrolyte

We prepared composite graphite electrodes without any additive (DAG87:super P:PVdF=90:5:5 in wt. ratio) as mentioned above. 2032-type two-electrode coin cells were assembled with Li foil (Cyprus Co., as a counter electrode) and a separator which is a trilayer of PP-PE-PP (polyethylene, polypropylene, Celgard). 2 wt. % of allyl sulfide (AS) additive (Fig. 1) was added to the 1.3 *M* $LiPF_6$ dissolved in the solvents mixture (EC:EMC:DEC = 3:2:5 in vol. ratio). As a reference, a coin cell using a background electrolyte without additive was also fabricated.

3.1.2. Galvanostatic Lithiation/De-lithiation Cycling Test

Lithiation/de-lithiation measurement and cycling were performed with a Wonatech battery cycler (WBCS3000). The assembled coin cells were pre-cycled 5 times at room temperature (25^{o}C) to generate stable solid electrolyte interphase (SEI) films on the graphite electrode. The pre-cycling steps were done at 37.2 mA g^{-1} (0.1 C-rate) for the 1st cycle and 74.4 mA g^{-1} (0.2 C-rate) for the remaining 4 cycles to the cutoff potentials of 0.005 and 2.0 V (*vs.* Li/Li^{+}) (Fig. 4). For lithiation, a constant-potential (0.005 V *vs.* Li/Li^{+}) step to the current limit of 18.6 mA g^{-1} was added subsequent to the constant-current lithiation. For the cycle test at the low-temperature condition (-30^{o}C), the cell was cycled at a current density of 18.6 mA g^{-1} in the same potential range at room temperature without a constant-potential step.

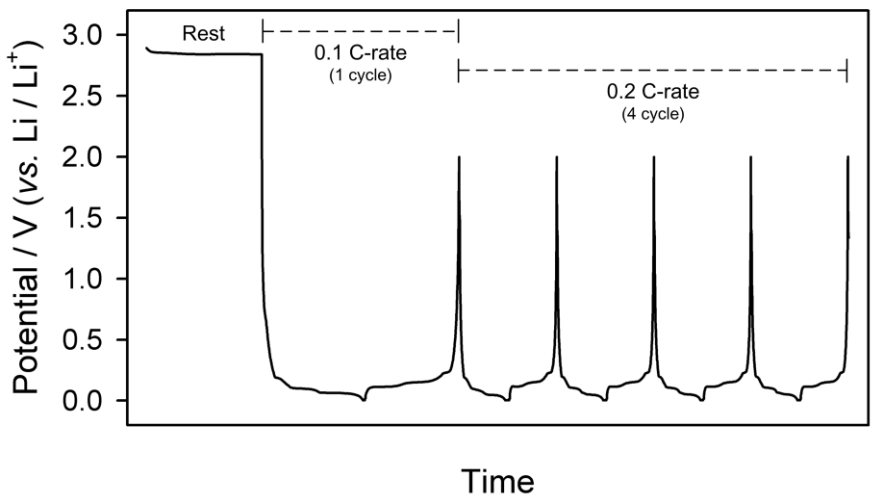

Fig. 4. Pre-cycling procedure of graphite electrode. The pre-cycling steps were done at 37.2 mA g^{-1} (0.1 C-rate) for the 1st cycle and 74.4 mA g^{-1} (0.2 C-rate) for the remaining 4 cycles to the cutoff potentials of 0.005 and 2.0 V (*vs.* Li/Li^+) (). For lithiation, a constant-potential (0.005 V *vs.* Li/Li^+) step to the current limit of 18.6 mA g^{-1} was added subsequent to the constant-current lithiation.

3.1.3. Li Plating Test

For the test of lithium plating, the cells were pre-cycled 5 times at 25^{o}C as described above and lithiated to 0.1 V (*vs*. Li/Li^{+}), which corresponds to 50% of the state of charge (SOC). After stabilized, the open circuit voltage of the cells is around 0.12 V. Then, a sequential current pulse and rest is applied by changing working temperature with the other being fixed. A typical pulse chain is represented in Fig. 5a. Here, a series of current pulse comprising a de-lithiation current pulse (10 C-rate) for 10 s, 3 hr rest, a lithiation current pulse (10 C-rate) for 10 s, and 6 hr rest is repeated while the cell temperature is changed from 25^{o}C to -30^{o}C at a cooling rate of 0.6^{o}C h^{-1}. As shown in a voltage transient (Fig. 5b), the potential of graphite electrode rises sharply upon de-lithiation pulse, but returns back to the equilibrium value (~0.1 V *vs*. Li/Li^{+} for 50% of SOC) during the subsequent rest period. Similarly, the electrode potential drops down immediately after a lithiation pulse, but returns back to the initial equilibrium value during the rest. Lithium plating was assessed by analyzing the voltage transients at the 6 hr rest period after the lithiation pulse and during the 10 s lithiation/de-lithiation current pulse period.

3.1.4. Electrochemical Impedance Spectroscopy (EIS)

The AC impedance of the cells was measured with an IM6e (Zahner) electrochemical station. The symmetric cell method [64,65] was adopted for the experimental valuation of the resistance without interruption of the Li counter electrode. The conditions for the EIS test were as follows. First, two identical

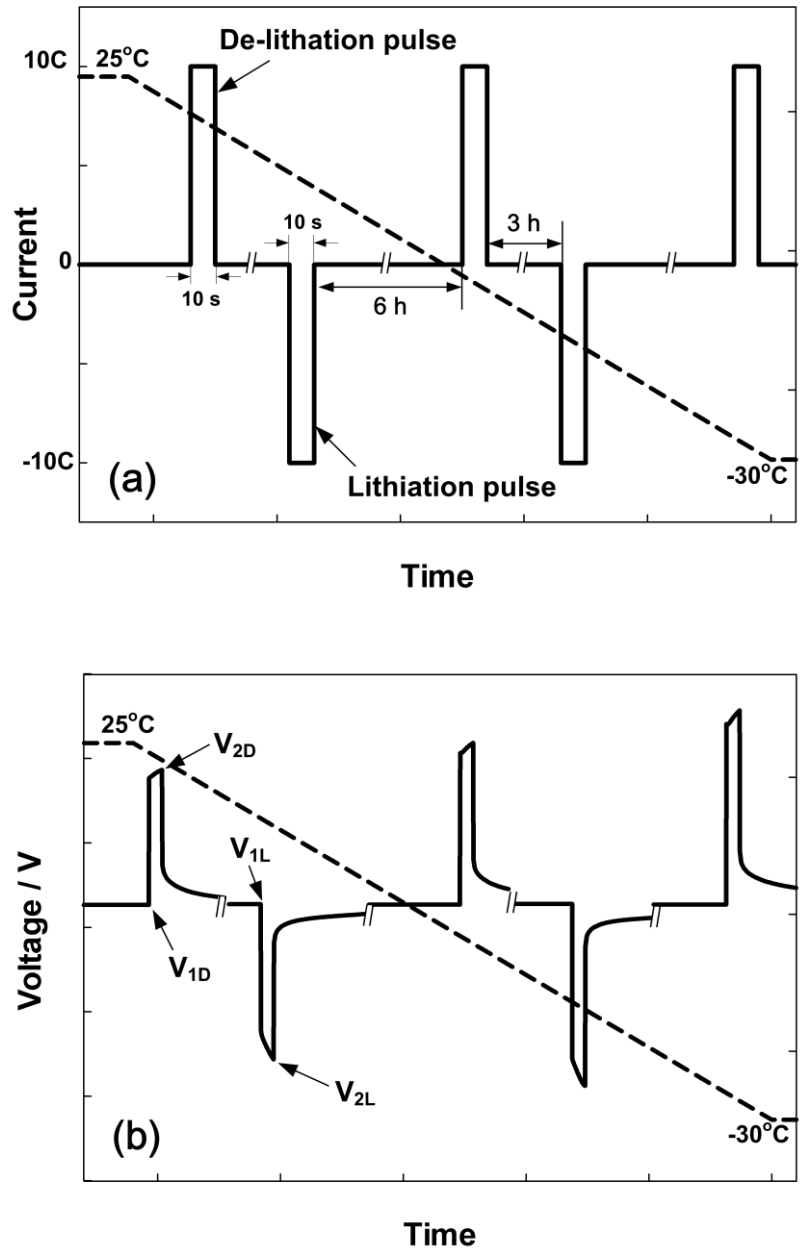

Fig. 5. (a); The test scheme comprising a series of discharge/charge current pulse (10*C*) and rest period with a variation in working temperature, and (b); the corresponding voltage transient.

electrodes were pre-cycled and lithiated to 0.1 V (*vs.* Li/Li^+) and kept constant until the current decayed to 18.6 mA g^{-1}. Then, two cells were disassembled in an argon-filled glove box and two identical graphite electrodes were collected. After washed with DEC, two electrodes were assembled again into a symmetric cell using the fresh background electrolyte (1.3 *M* $LiPF_6$ in EC:EMC:DEC = 3:2:5 in vol. ratio). EIS measurements were performed with a 5 mV amplitude excitation, from 100 kHz to 50 mHz. All the impedance parameters are reported in normalized impedances (Ω g).

3.2. Reactivity Test

3.2.1. Chemical Reactivity Test (Elemental Sulfur Additive)

In order to confirm the chemical reaction between lithium polysulfide (Li_2S_8) and carbonate solvents, Li_2S_8 was prepared by a reaction between lithium metal and sulfur (S_8) in EC and DEC (Fig. 6) [66]. Elemental sulfur (S_8) and lithium metal were mixed with the carbonate solvents (EC and DEC, 50 mmol) and stirred for 48 hr at 40°C (EC) and 25°C (DEC). After 48 hr, the solutions became colored. After that, 2 wt. % of each products were added separately to the background electrolyte (1.3 *M* $LiPF_6$ in EC:EMC:DEC = 3:2:5 in vol. ratio) and their electrochemical properties (reductive decomposition and surface film formation) were examined by cyclic voltammetry on a glassy carbon electrode with a lithium metal reference. The cutoff potentials of the cyclic voltammetry were 0.2 V and 2 V (*vs.* Li/Li^+) and the scan rate was 0.01 mV s^{-1}.

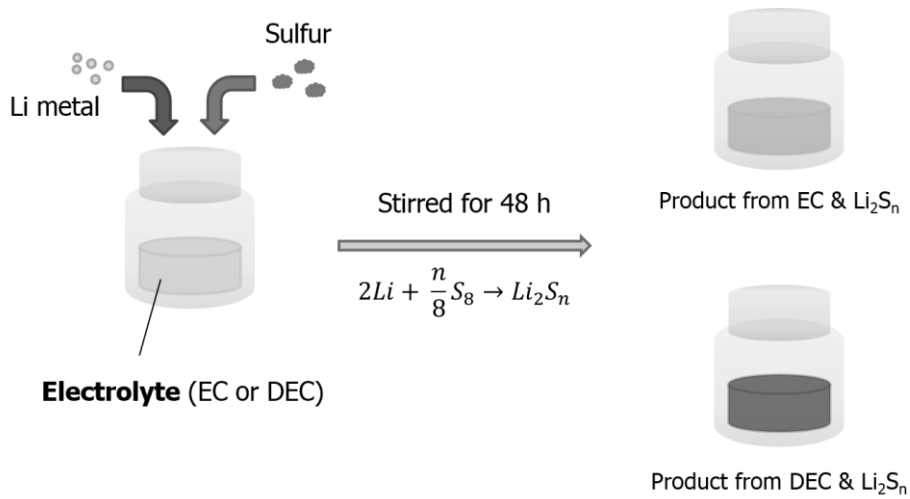

Fig. 6. Preparation of thiocarbonates by reactions between lithium metal and sulfur (S_8) in electrolyte solvents (EC and DEC).

3.2.2. Open Circuit Voltage Measurement (Allyl Sulfide Additive)

The open circuit voltage (OCV) of the cells was measured using a Wonatech battery cycler (WBCS3000). After assembled in a glovebox (under Ar atmosphere), the cells were rested 12 hr for stabilization and the OCV of the cells was checked after this rest step.

3.3. Properties of Solid Electrolyte Interphase (SEI) Film

3.3.1. X-ray Photoelectron Spectroscopy (XPS)

For the X-ray photoelectron spectroscopy (XPS) analyses, the tested cells were disassembled in a glovebox (under Ar atmosphere), and the cycled electrodes were collected and washed with DEC. A hermetic vessel was used to transfer the electrode samples from the glovebox to the XPS instrument chamber without air exposure. The photo electrons were excited using Al Kα (1486.6 eV) radiation at a constant power of 150 W (15 kV and 10 mA) with an X-ray spot size of 400 μm^2. During data acquisition, a constant-analyzer-energy mode was used at a pass energy of 30 eV and a step of 0.1 eV. The depth-profiling of the film was made by continued Ar ion sputter etching. The binding energy was calibrated using the C 1s peak at 285.0 eV.

3.3.2. Field-emission Scanning Electron Microscope (FE-SEM)

For the field-emission scanning electron microscope (FE-SEM, JSM-6700F,

JEOL), the cells were disassembled in a glovebox (under Ar atmosphere), and the electrodes were collected and washed with DEC. A hermetic vessel was also used to transfer the samples to the FE-SEM instrument with minimum air exposure.

4. RESULTS AND DISCUSSION

4.1. Elemental Sulfur Additive for Electrode

4.1.1. Film-forming Mechanism

4.1.1.1. Electrochemical Behavior during Pre-cycling

The lithiation/de-lithiation profiles of the sulfur-added cell and the sulfur-free one at the 1st cycle are shown in Fig. 7. Two cells show similar behavior, except that there is an additional charge consumption between 0.7~2 V (*vs.* Li/Li^+) in the sulfur-added cell. The Coulombic efficiency of the sulfur-added cell is 89.7 % which is somewhat lower than that of the sulfur-free one (93.0 %), indicating an irreversible reaction related with elemental sulfur additive is occurred at 1st cycle.

In order to address this reaction of elemental sulfur in the graphite electrode, the dQ/dV plots of the 1st lithiation step of the two cells are compared in Fig. 8. At first glance, there appears a distinctive peak at 1.68 V (vs. Li/Li^+) on the dQ/dV plot obtained from the sulfur-added electrode (Fig. 8a). This peak implies the possibility that copper sulfide (CuS or Cu_2S) is formed on the surface of current collector, which is copper metal foil, by a reaction between copper and some of the elemental sulfur additive [67,68]. According to previous studies [69-71], there are two defined plateaus (in the lithiation step) at 2.1~1.8 V for CuS and at ~1.8 V for Cu_2S.

The electrochemical reactions associated with the cleavage of elemental sulfur can be found near 2.0 V (*vs.* Li/Li^+) [72,73]. It is known that sulfur (S_8) is cleaved

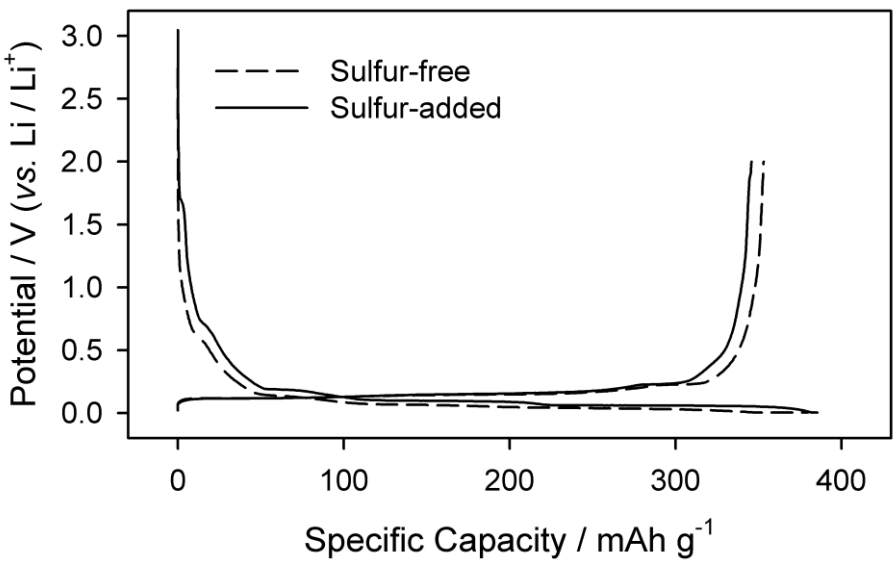

Fig. 7. Comparison of the lithiation/de-lithiation characteristics of the Li/graphite cell in which the sulfur-added and sulfur-free graphite electrodes at 1st cycle.

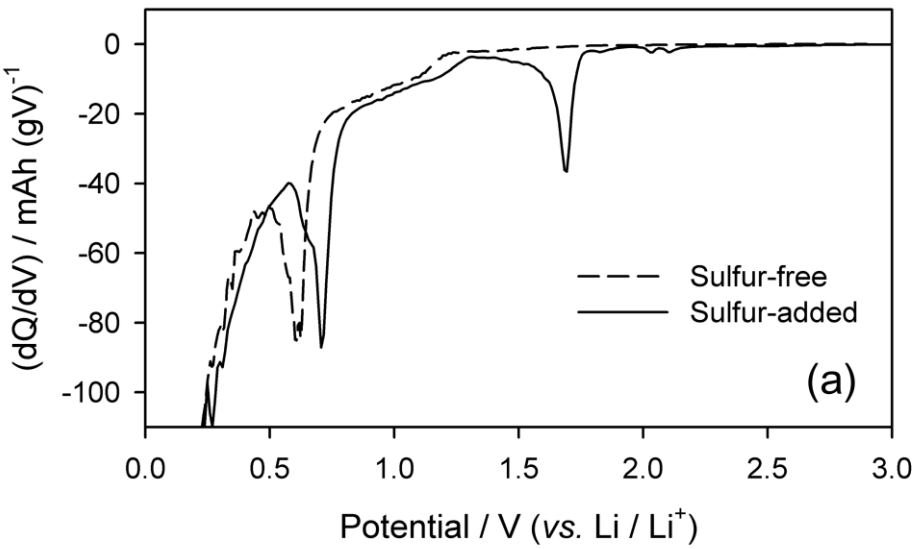

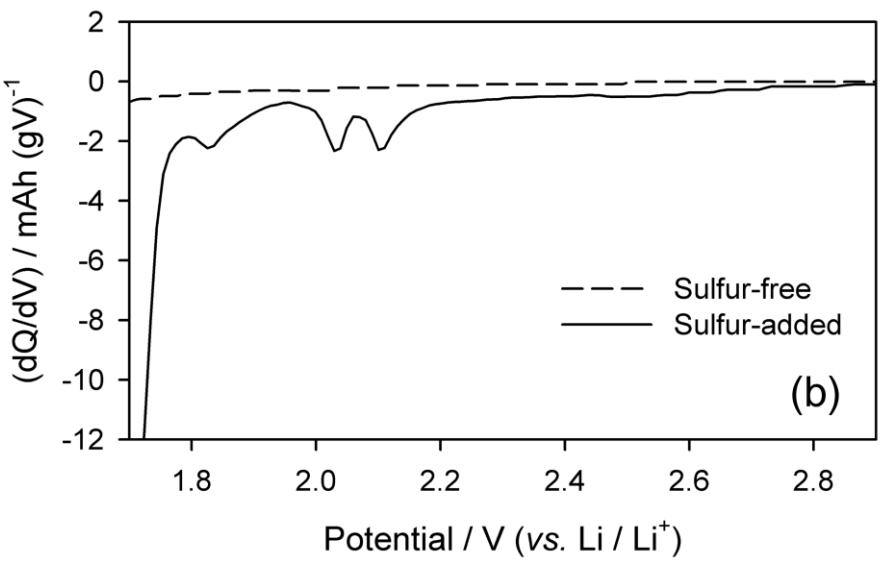

Fig. 8. Differential capacity plot (dQ/dV) for the 1st lithiation step at 25°C: (a) full-range; (b) magnification of dQ/dV plot between 1.7~2.9 V (reduction of elemental sulfur).

by electrochemical reduction near 2.1 V to produce an intermediate in the form of lithium polysulfide (Li_2S_8) [72,73]. The peak at 2.1 V (Fig. 8b) in the dQ/dV plot, which appeared only from the sulfur-added electrode, can be attributed to the formation of Li_2S_8. Unlike ether-based electrolytes which are generally used in Li-S cells, it is known that carbonate-based electrolytes exhibit side reactions with Li_2S_8 and generate intermediates including thiocarbonate species [72,74,75]. It should be noted that the formation of thiocarbonates is a solution-phase chemical reaction, not an electrochemical one.

There are two other peaks around 1.7~2.0 V, believed to be related with the electrochemical reduction of as-generated thiocarbonate intermediates on the graphite surface (Fig. 8b). To confirm this, a control experiment was performed, in which Li_2S_8 was prepared and mixed with an electrolyte solvent (EC or DEC) to form the intermediates. After reactions completed, 2 wt. % of each as-generated intermediates, which must be thiocarbonates as reported in the literatures [72,74,75], was added to the background electrolyte and examined with cyclic voltammetry. Fig. 9a shows the cyclic voltammograms (CV) obtained from the background electrolyte. The reductive decomposition of the background electrolyte is appeared at <1.0 V in the 1st negative scan and disappeared in the 2nd scan (passivation on glassy carbon electrode). Compared to the background electrolyte, the voltammograms from the other two electrolytes (Fig. 9a and c), into which the as-generated thiocarbonates are separately added, display additional significant reduction current overlapped on the reduction current of the background electrolyte. The thiocarbonates that are generated from Li_2S_8 and EC show peaks at ~2.0 V and ~1.5 V, and the reduction behavior at a wide range (0.5~2.2 V) (Fig. 9b), whereas

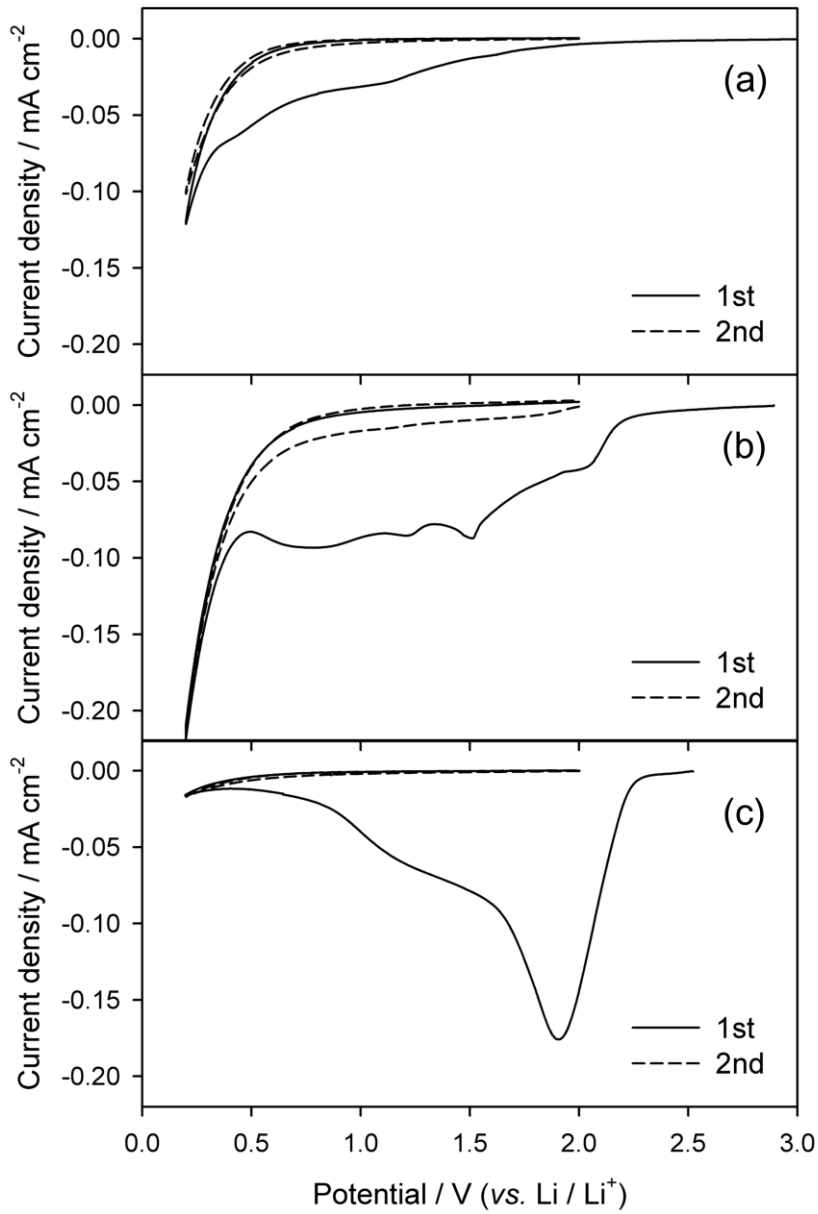

Fig. 9. Cyclic voltammograms traced in: (a) the background electrolyte (1.3*M* $LiPF_6$ in EC:EMC:DEC=3:2:5 (v/v)), (b); the background electrolyte along with the products of Li_2S_8 and EC, and (c); the background electrolyte along with the products of Li_2S_8 and DEC. Working electrode = glassy carbon. Reference electrode = lithium metal. Scan rate = 0.01 V s^{-1}.

those generated from Li_2S_8 and DEC show a large and broad reduction peak at ~1.9 V and also broad reduction current at 1.0~2.2 V (Fig. 9c). From this control experiment, the reduction peaks at 1.7~2.0 V in Fig. 8b can be accounted for by the decomposition of thiocarbonate intermediates that are generated by the solution-phase chemical reaction between Li_2S_8 and EC or DEC. The reduction peaks corresponding to the decomposition of the background electrolyte are found below 0.8 V in Fig. 8a. The peak of the sulfur-added electrode appears at 0.7 V, which is about 0.1 V higher than the sulfur-free electrode. There are two possible explanation for this phenomenon. First, there is a possibility of a subsequent reduction of the thiocarbonates described above. Second, the pre-formed film on the graphite surface might reduce the resistance of the electrode and help solvent decomposition occur earlier. Because the peaks of the sulfur-added electrode corresponding to Li insertion into the graphite structure are seen at a higher potential than those of the sulfur-free electrode (Fig. 10), the latter explanation appears to be more plausible.

4.1.1.2. Form of Sulfur Compounds during Pre-cycling

To gain an understanding of the mechanism of film formation with the elemental sulfur additive, the change in chemical composition of the surface film was analyzed with XPS. The S 2p spectra are shown in Fig. 11. Before cycling, sulfur exists in the form of elemental sulfur (S_8, 164.0 eV) [76] in the graphite electrode. During cycling, the form of sulfur compounds can be divided into three regions in the S 2p spectra. The obtained XPS data are analyzed according to the

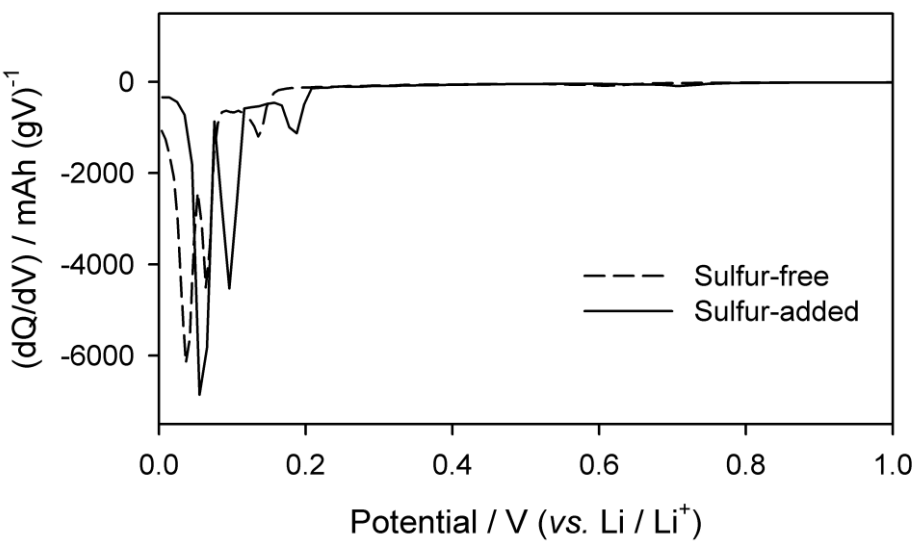

Fig. 10. Differential capacity plot (dQ/dV) for the 1st lithiation step at 25°C: magnification of dQ/dV plot between 0~0.5 V (electrolyte solvent decomposition).

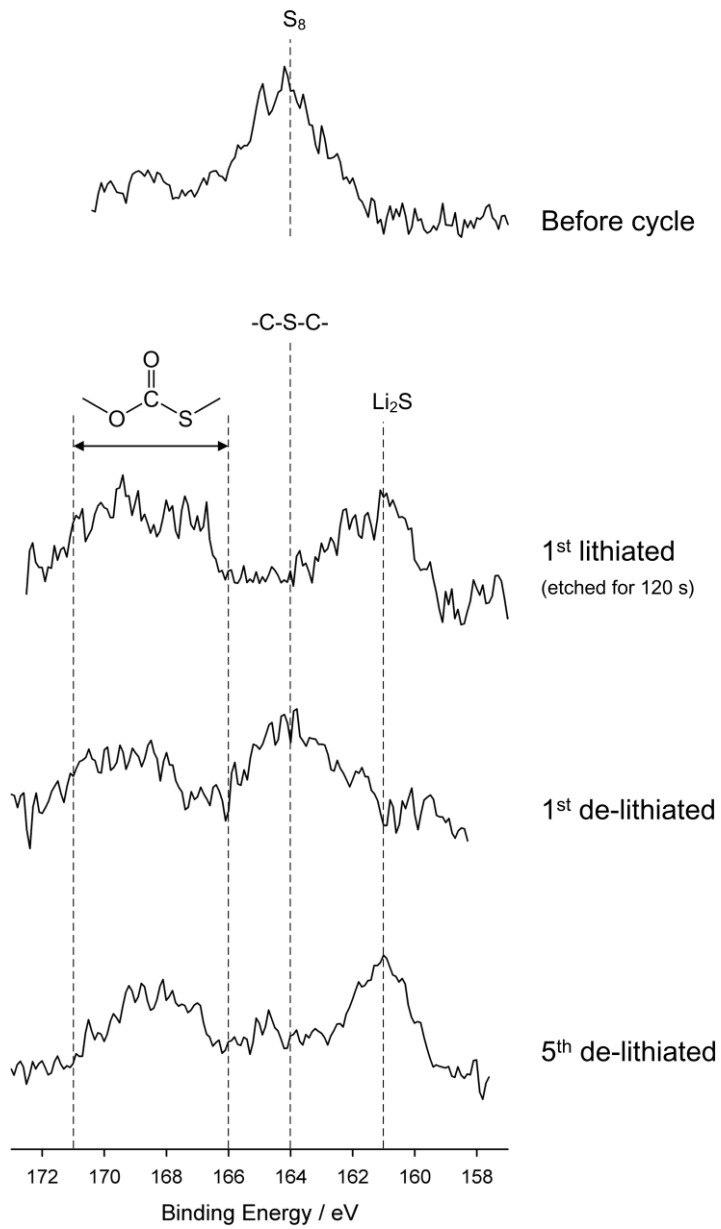

Fig. 11. S 2p XPS spectra obtained from the sulfur-added graphite electrode during pre-cycling.

reported binding energy values. The peak at 161 eV is considered to be Li_2S [76,77]. It is more reasonable to assign the peak at 164.0 eV to the sulfide bond (-C-S-C) [76,77] than to elemental sulfur after 1st cycle because it is difficult for sulfur compounds to be converted into elemental sulfur again within the cutoff range (0.005~2.0 V *vs.* Li/Li^+). The peaks around 166~171 eV can be assigned to the thiocarbonate species (-O-CO-S) [78].

After 1st lithiation, the sulfur-derived film is found in the deeper region (after 120 s etching) of the film, but the outer region is covered by the sulfur-free film that are derived from background electrolyte. The sulfur-derived film in this step contains Li_2S and thiocarbonate species. These compounds appear during the subsequent step, implying that the thiocarbonates species are stable against electrochemical oxidation and reduction. The sulfide (-C-S-C-) species that appear from the 1st de-lithiation also seem to be stable, as this peak appears in the forthcoming step. From the results, it can be concluded that these two types of compounds are stable and can passivate the surface of graphite. As is seen in Fig. 11, however, Li_2S that is generated in the 1st lithiation disappears upon the forthcoming de-lithiation. This feature can be explained by the electrochemical oxidation of Li_2S into lithium polysulfides (Li_2S_4 or Li_2S_8) in the 1st de-lithiation period. It should be noted that Li_2S is insoluble in the carbonate solvents, whereas Li_2S_4 and Li_2S_8 are soluble so can be dissolved into the electrolytes. The intense peak of Li_2S observed after the 5th de-lithiation must be due to the fact that the Li_2S at the topmost region cannot be electrochemically oxidized because of the intervening surface film that grows to a certain thickness during previous 5 cycles. That means, the insoluble Li_2S can remain at the topmost region of the surface

films. Fundamentally, surface films are insulating, implying that electron tunneling is impossible if surface films grow up to a certain thickness. After the pre-cycling (5^{th} de-lithiation), the SEI film carries the sulfur compounds such as Li_2S, sulfides, and thiocarbonate species in it.

The deposition of Li_2S upon lithiation and disappearance upon de-lithiation are further confirmed using the dQ/dV plots shown in Fig. 12. For the sulfur-added electrode, there are additional oxidation peaks in the 1^{st} de-lithiation step (Fig. 12a). The distinctive peak appeared at 1.9 V (*vs.* Li/Li^+) can be assigned to the electrochemical oxidation of Li_2S into lithium polysulfides (Li_2S_x, x=4~8) [72]. The soluble lithium polysulfides then react with the carbonate solvents to generate the thiocarbonate species that are electrochemically decomposed to form surface films. The deposition of Li_2S and dissolution as a form of lithium polysulfides can be repeated until the graphite surface is fully passivated. The absence of 1.9 V peak after 5^{th} de-lithiation (Fig. 12b) signifies the passivation of graphite surface.

The insoluble Li_2S remains in the surface films after the 5^{th} de-lithiation (Fig. 11) because the oxidation to the soluble Li_2S_x (x = 4-8) is suppressed due to the passivation. There is, meanwhile, a broad additional oxidation peak is showed around 0.3~0.5 V (*vs.* Li/Li^+) Fig. 12, indicating that an unstable film related with sulfur compounds is electrochemically oxidized at 1^{st} de-lithiation. This dissolution is also disappeared after 5^{th} de-lithiation, which means the stable SEI film is developed on the graphite surface.

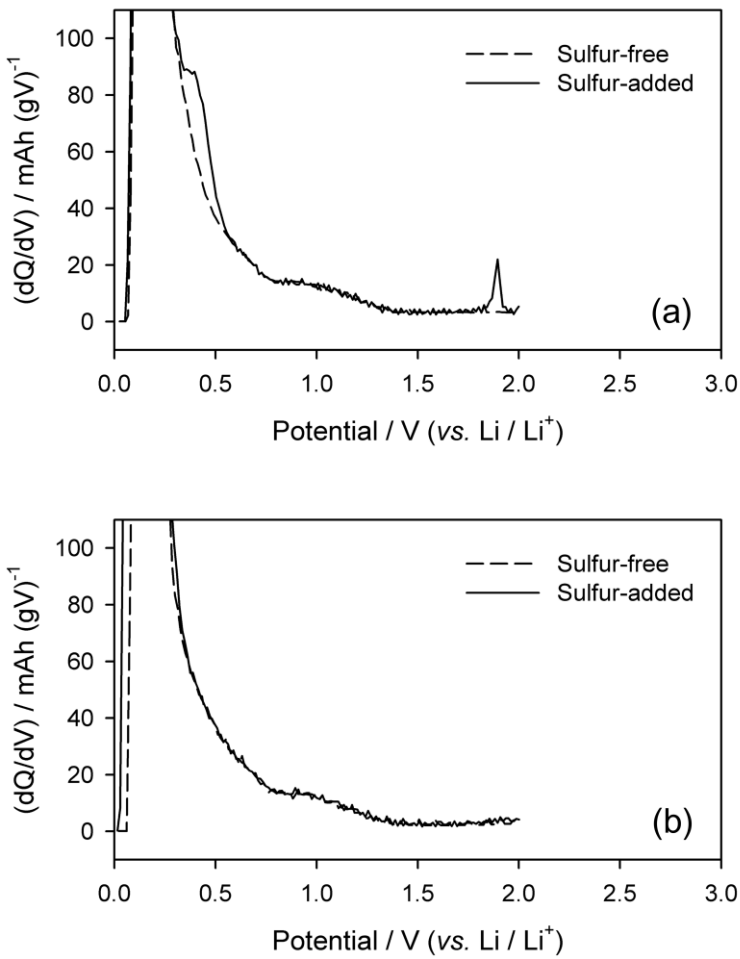

Fig. 12. Differential capacity plot (dQ/dV) for (a) the 1st de-lithiation step in the pre-cycling stage and (b) the 5th de-lithiation step.

4.1.1.3. Chemical Aspects of the SEI Chemistry

Fig. 13 presents the C 1s, O 1s and F 1s core peaks of two surface films after 5th de-lithiation. The enriched portion of carbon-oxygen species in this film is confirmed by the O 1s spectra. As shown in Fig. 13, the O 1s spectra are fitted with four broad peaks centered at 528.5 eV (Li_2O), 531 eV (LiOH), 532 eV (Li_2CO_3 or O-C=O), and 533.5 eV (O-C=O) [79-83]. As seen, surface film from sulfur additive gives rise to a higher intensity for the carbon-oxygen species at 532 eV and 533.5 eV. Furthermore, the peak at 528.5 eV which is attributed to Li_2O is decreased in the sulfur-added film. In contrast to the enrichment of carbon-oxygen species, the population of inorganic fluorinated species (mainly LiF) from salt compound ($LiPF_6$) is lower in sulfur-derived film. The F 1s spectra are fitted with three peaks comprised of LiF (685.1 eV), $Li_xPF_yO_z$ (686.6 eV), and $LiPF_6$ or CF_2 (688 eV) [82,83]. Especially LiF is dominant over the other F-species in the sulfur-free film.

The two surface films show differences in chemical composition through the depth, as shown in the depth-profiling XPS data (Fig. 14). When the atomic concentration of four elements are plotted as a function of etching time, the sulfur free film display plenty of F-species in the deeper region (Fig. 14a), whereas C-species is dominant in the sulfur-derived film (Fig. 14b). It indicates that the inner SEI films close to the electrode surface have different characteristics. Before other electrolyte components are reduced, the film forming agents from elemental sulfur (ex. thiocarbonates) react on the graphite surface and build the inner surface film. Therefore, it can be expected that this pre-formed film covers the bare graphite and

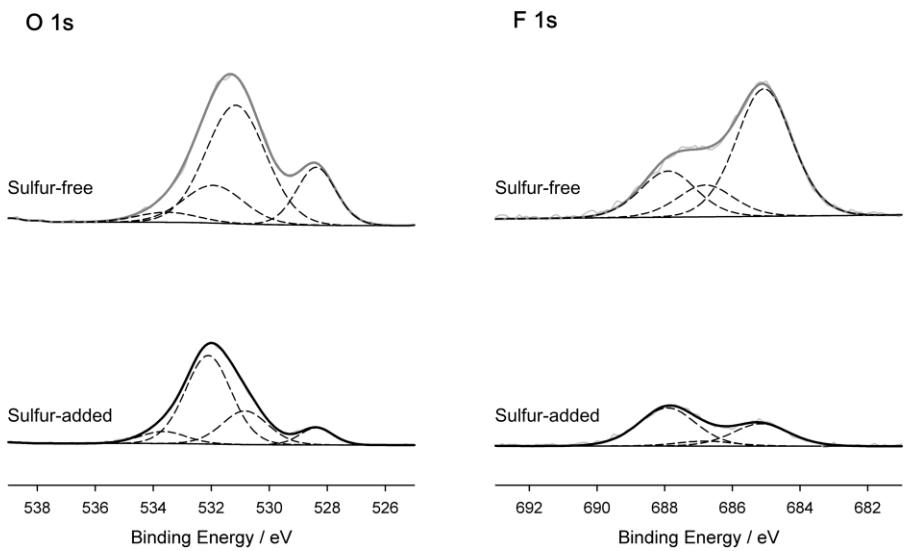

Fig. 13. O 1s and F 1s XPS spectra obtained from the topmost surface of the sulfur-free and the sulfur-added graphite electrodes.

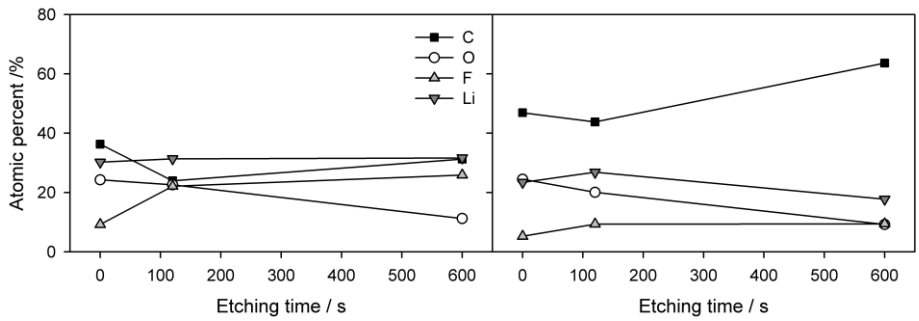

Fig. 14. The variation of chemical composition as a function of film depth of (a) the sulfur-free and (b) the sulfur-added film. The results were obtained by fitting the depth-profiling XPS data. The measurement was made after 5^{th} de-lithiation.

prevents $LiPF_6$ salt decomposition on the graphite surface. (It is known that salt decomposition induces LiF formation [84].) The carbon-oxygen species must come from the carbonate solvent (EC, DEC, and EMC in this work) or sulfur compounds containing carbonate-like functional groups. Since it is reported that sulfur-containing additive makes SEI with higher C-O and smaller LiF contributions [85], it seems that sulfur compounds are the more probable sources in the early stage of SEI formation and affect the subsequent SEI formation step. The morphology of SEI films of two electrodes are quite similar, as shown is Fig. 15.

Based on all the results, we propose a mechanism for the film-forming process with elemental sulfur depicted by the schematic in Fig. 16. The film-forming process can be divided into three stages: (i) Around 2.1 V, the elemental sulfur is electrochemically reduced and turns into the soluble polysulfide (Li_2S_8); (ii) the polysulfide (Li_2S_8) chemically reacts with EC, EMC, and DEC to produce a variety of thiocarbonate species in solution, some of which are represented in Fig. 16; and (iii) the as-generated thiocarbonates are then electrochemically decomposed to produce the sulfur-containing compounds (Li_2S, -C-S-C-, and -O-CO-S-), which are deposited on the electrode surface.

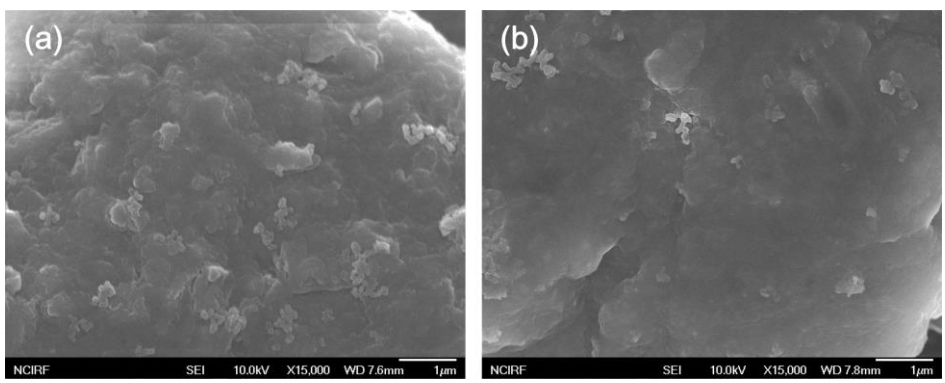

Fig. 15. FE-SEM image of (a) the sulfur-free and (b) the sulfur-added graphite electrode after pre-cycled.

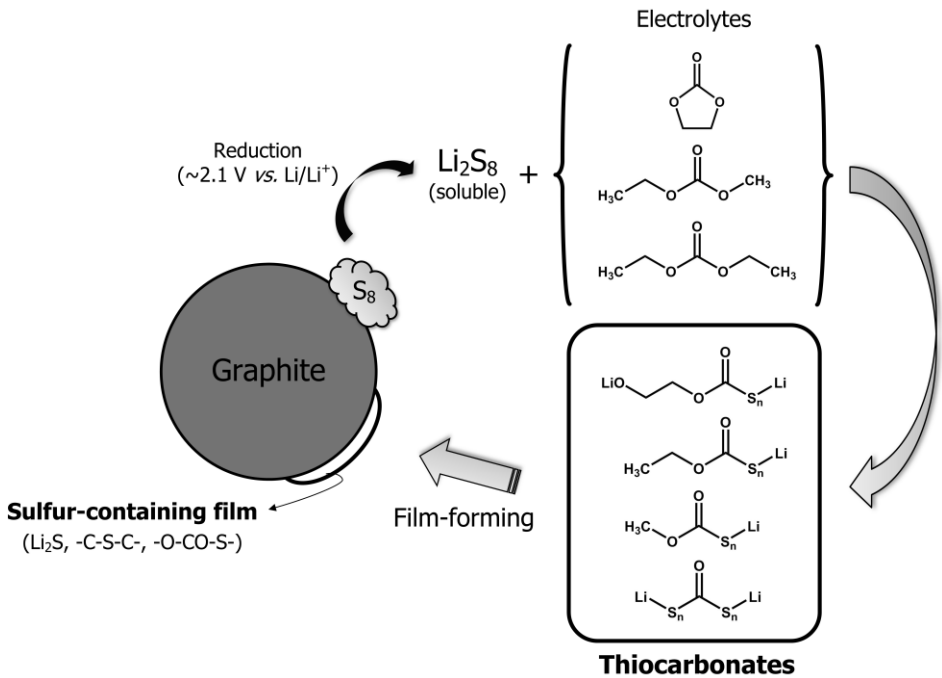

Fig. 16. Schematic illustration for the film-forming process: From the elemental sulfur to the sulfur-containing surface film.

4.1.2. Low-temperature Performance

4.1.2.1. Lithiation/De-lithiation Performance

Fig. 17 compares the reversible capacity for two Li/graphite cells, into which the sulfur-added and sulfur-free graphite electrode were loaded separately. At room temperature (25^{o}C), the two cells exhibit a comparable behavior with respect to the reversible capacity (~365 mAh g^{-1}) and Coulombic efficiency (~99%), suggesting that a desirable SEI film is formed on both graphite electrodes. It should be noted that the elemental sulfur additive does not exhibit any severe unfavorable effects that would limit the reversible capacity or efficiency. When the cells described above were tested at low-temperatures (-10^{o}C at a 0.2 C-rate and -30^{o}C at a 0.05 C-rate), as shown in Fig. 17, the electrode with the sulfur additive exhibits enhanced low-temperature performances below zero temperatures, especially the reversible capacity is almost twice as large as the one for the sulfur-free one at -30^{o}C. Notably, the Coulombic efficiencies of both cells can reach ~98% even at -30^{o}C, illustrating that once the Li ions are inserted into graphite structure, they can easily move out even in severe low-temperature conditions. To ascertain this feature, a control experiment was performed with the sulfur-free cell, in which the lithiation was carried out at 25^{o}C but de-lithiation at -30^{o}C (Fig. 18). The result shows that the de-lithiation capacity at -30^{o}C is almost the same with the lithiation capacity at 25^{o}C, demonstrating that the intercalated Li^{+} ions are fully removed even at low temperatures, which further implies that the lithiation process limits the low-temperature performance of graphite electrodes. Because the major lithiation takes place close to the cutoff potential (0.005 *vs.* Li/Li^{+}), the lithiation capacity is

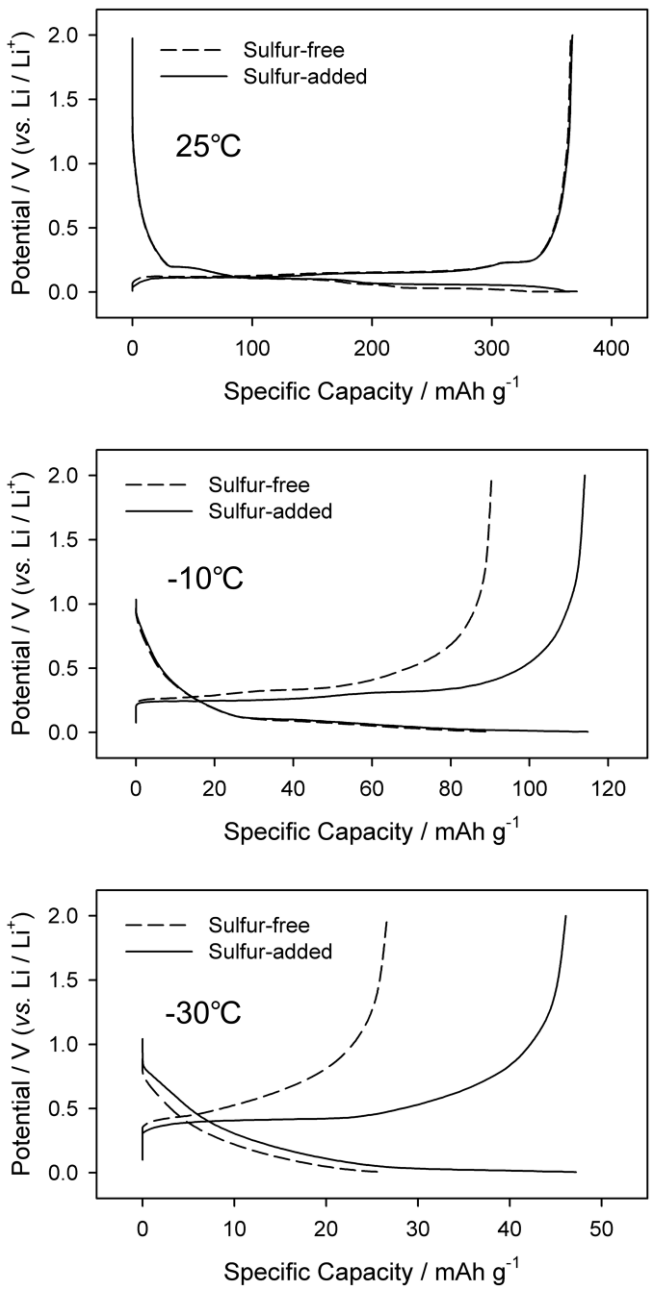

Fig. 17. Comparison of the reversible capacity for two Li/graphite cells, into which the sulfur-added and sulfur-free graphite electrode were loaded separately. The cells were pre-cycled five times at 25°C before the test. Voltage cutoff = 0.005~2.0 V. Current density = 74.4 mA g^{-1} (0.2 C-rate) at 25°C, -10°C and 18.6 mA g^{-1} (0.05 C-rate) at -30°C.

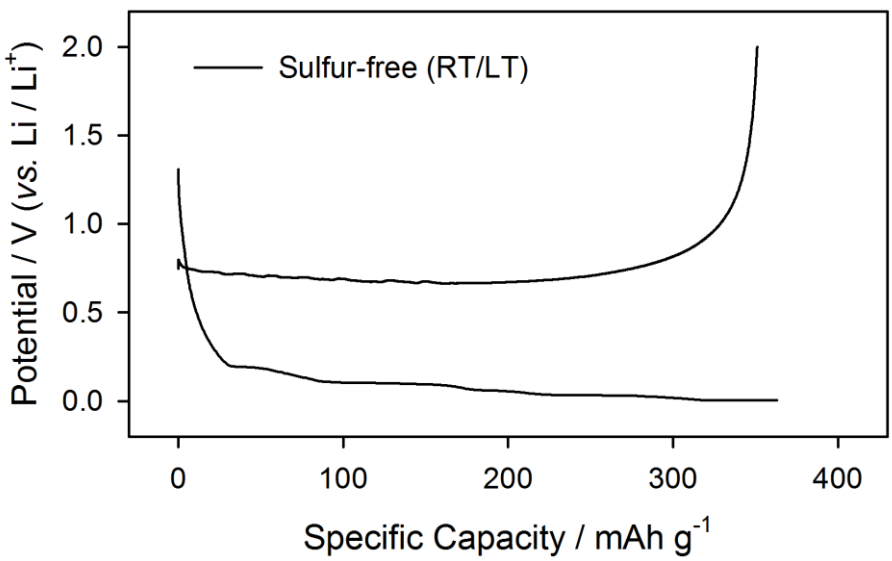

Fig. 18. Lithiation/de-lithiation behavior of the sulfur-free graphite electrode that is fully lithiated at 25^{o}C and de-lithiated at -30^{o}C (0.2 C-rate).

sensitively affected by the cell polarization; a slight difference in cell polarization brings about a significant difference in the lithiation capacity, and thus the de-lithiation capacity and further the reversible capacity.

Meanwhile, the superior low-temperature performance given by the sulfur-added cell was maintained even after a long-term cycling. Both the sulfur-free and sulfur-added cells were cycled for 50 cycles at room temperature and then tested at -30^{o}C. Fig. 19a shows the 0.5 C-rate cycle performance of two cells. Two cells exhibit a comparable capacity retention up to 50 cycles. The low-temperature charge-discharge performance of the sulfur-added cell is still superior to the sulfur-free one (Fig. 19b).

4.1.2.2. Li Plating (Pulse Test)

The voltage values at the end of de-lithiation pulse (V_{2D}) with respect to the initial equilibrium value were calculated and the voltage difference ($\triangle V_D = | V_{1D} - V_{2D}|$) is plotted as a function of temperature in Fig. 20a. The voltage difference ($\triangle V_L = |V_{1L} - V_{2L}|$) obtained from the lithiation pulse is displayed in Fig. 20b. As seen, the voltage difference for the sulfur-added cell is much smaller in both cases, implying that the overpotential for the sulfur-added graphite electrode is smaller than that for the sulfur-free graphite. It should be noted the voltage difference from the lithiation pulse is significantly higher than de-lithiation, which indicates lithiation into the graphite is more difficult, in accordance with previous results (Fig. 18). During the pulse test, Li^+ intercalation/de-intercalation is made within a

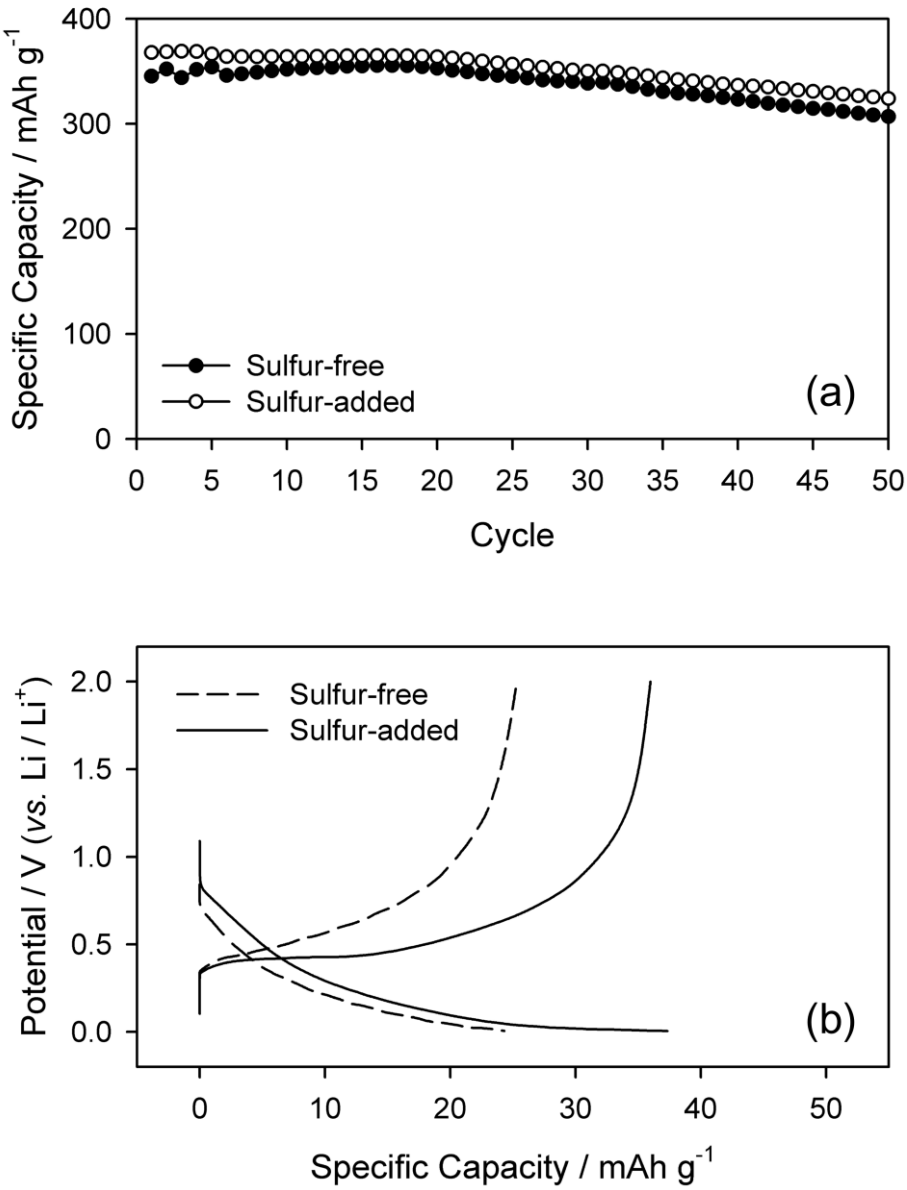

Fig. 19. (a) Cycle performance of Li/graphite cells (0.5 C-rate, 25^{o}C) and (b) Comparison of the reversible capacity for two Li/graphite cells at -30^{o}C after the cycling (0.05 C-rate).

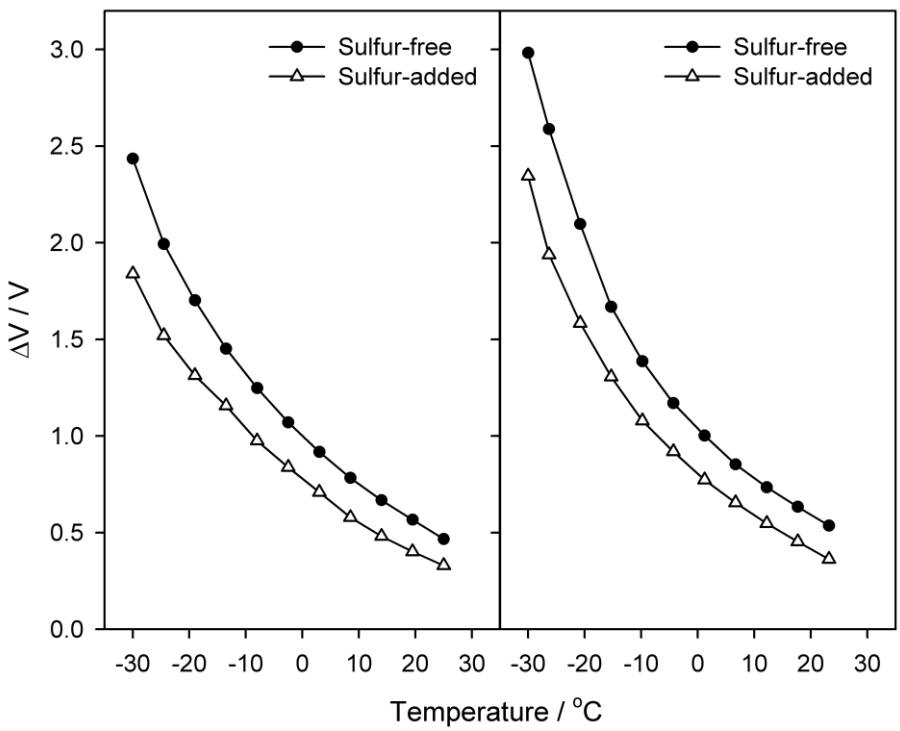

Fig. 20. A comparison of voltage difference ($\Delta V = |V_1 - V_2|$) for the (a) de-lithiation (ΔV_D) and (b) lithiation current pulse (ΔV_L) as a function of temperature (25~-30°C) at a fixed pulse height (10 C-rate).

narrow range of SOC (50 ± 2.8 %).

Fig. 21 shows the voltage transients obtained at the 6 hr rest period after the lithiation pulse (10 C-rate). At high temperatures (≥ 12.2^{o}C), the potential of the sulfur-free graphite electrode immediately restores back to the initial equilibrium value (~0.12 V *vs*. Li/Li^{+}). A similar voltage restoration is observed at lower temperatures (≤ -9.8^{o}C), but after giving rise to a voltage plateau (Fig. 21a). This voltage plateau represents the mixed potential and thus a signature for lithium plating.

Namely, the plated metallic lithium on the graphite electrode tends to be oxidized ($yLi \rightarrow yLi^{+} + ye$) during the rest period, and the graphite electrode is reduced ($Li_xC_6 + yLi^{+} + ye \rightarrow Li_{x+y}C_6$) by taking the released lithium ions (yLi^{+}) and electrons (ye). A local galvanic cell forms by these coupled electrochemical reactions, and the graphite electrode now shows a mixed potential that is pinned at the middle of two electrode potentials. With an increase in lithium plating, the mixed potential appears at a lower value (closer to the lithium plating potential) and its duration in the relaxation profiles is longer. All these features are clearly seen in Fig. 21a. That is, the profile obtained at the lowest temperature (-30^{o}C), under which condition the largest amount of lithium plating is expected, exhibits the lowest mixed potential that prevails for the longest period of time. In case of the sulfur-added graphite electrode (Fig. 21b), otherwise, the mixed potential is not clearly appeared even at -30^{o}C, indicating lithium plating is suppressed in the low-temperature conditions.

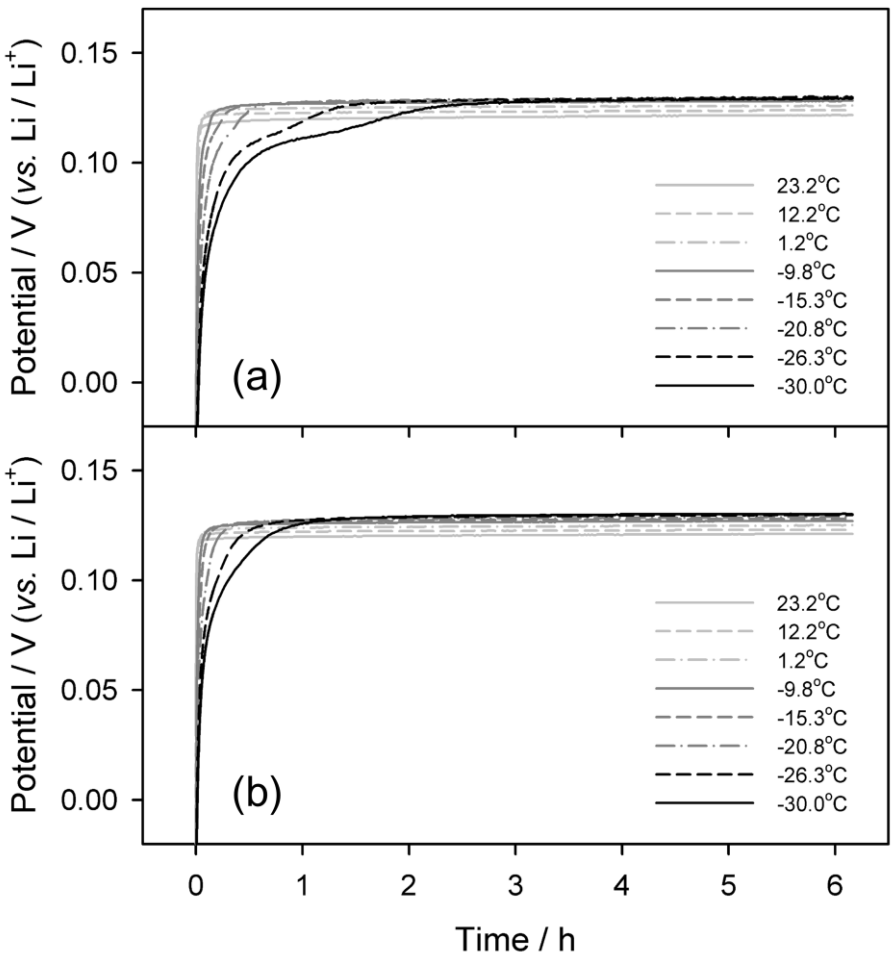

Fig. 21. The voltage relaxation profiles of (a) the sulfur-free graphite electrode and (b) the sulfur-added one during 6 hr rest period after a lithiation pulse (10 C-rate) at different temperatures. The temperature at the beginning of lithiation pulse is indicated in the inset.

4.1.2.3. Electrochemical Impedance Spectroscopy (EIS)

To unravel the origin of the less serious cell polarization in the Li/sulfur-added graphite cell, impedance analysis was performed. Fig. 22 displays the Nyquist plots and Table 2 lists the impedance parameters obtained by fitting the spectra with a Voigt-type equivalent circuit [86-88], which consists of resistors (R), constant-phase elements (CPE) as the substitute for capacitors, and a Warburg term (Z_W). As is seen in Fig. 22, the impedance spectra are characterized by two time-constants (semicircles) in the high to middle frequency region and by a slope at the low frequencies. The semicircle at the high-frequency region is assigned to the parallel combination of SEI resistance (R_{SEI}) and CPE components (capacitors) of the surface film, whereas the semicircle at the middle-frequency region is attributed to the combined feature of charge transfer resistance (R_{CT}) and double-layer capacitance (CPE_{dl}) [2,89]. As is listed Table 2, all the resistance values increase with a decrease in the working temperature. The values of R_Ω and R_{SEI} at -30^{o}C are about one-order of magnitude larger than those at 25^{o}C. In the same temperature range, however, the increase of R_{CT} is remarkable; the value at -30^{o}C is almost 300 times larger than that at 25^{o}C for the sulfur-free electrode, demonstrating that the charge transfer reaction between graphite and lithium becomes extremely difficult at low temperatures. At -30^{o}C, the charge transfer resistance accounts for most of the impedance (Fig. 23).

A comparison of the temperature-dependent resistance values for the two cells reveals at least two features. First, the resistance relevant to Li^+ transport through surface film (R_{SEI}) is slightly larger for the sulfur-added electrode, implying that

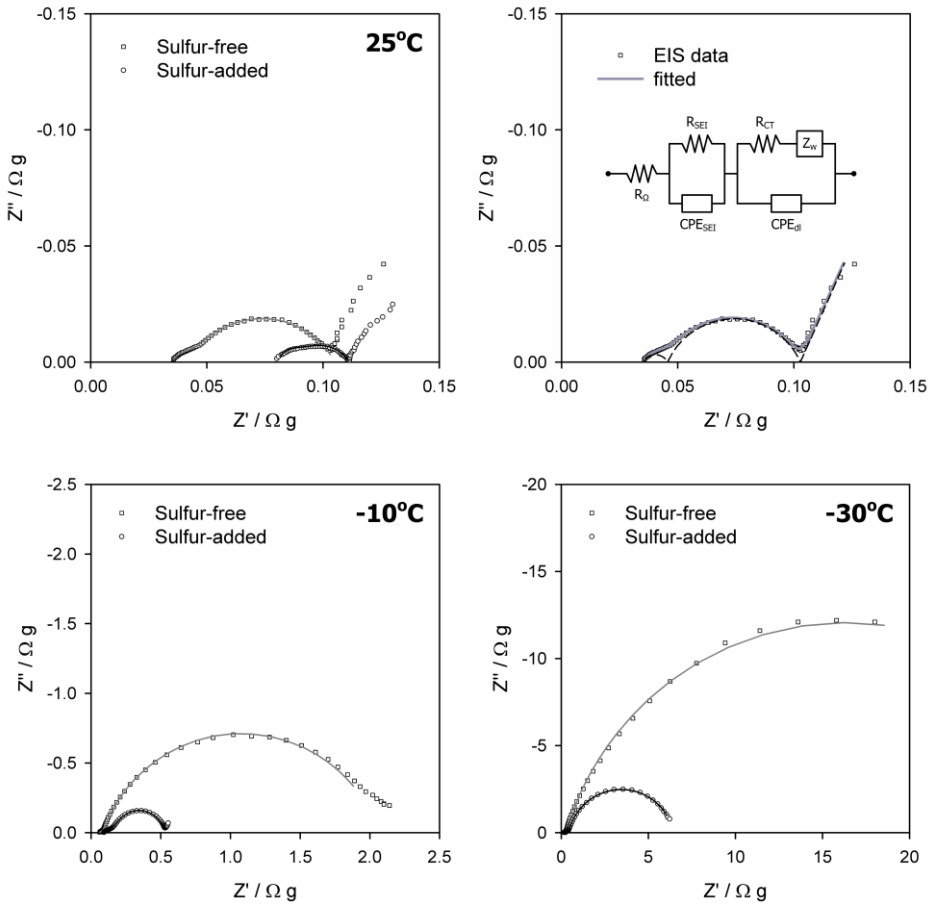

Fig. 22. The Nyquist plots obtained from the symmetric cells as a function of temperature. The typical fitting result performed with the equivalent circuit is represented at the upper-right corner.

	R_{Ω} (mΩ g)		R_{SEI} (mΩ g)		R_{CT} (mΩ g)	
Temperature (℃)	**Sulfur-free**	**Sulfur-added**	**Sulfur-free**	**Sulfur-added**	**Sulfur-free**	**Sulfur-added**
25	35.1 (± 0.2)	80.4 (± 0.2)	8.4 (± 0.5)	9.2 (± 0.8)	61.3 (± 0.6)	21.5 (± 0.9)
0	49.2 (± 0.3)	75.2 (± 0.2)	16.4 (± 0.7)	69.1 (± 0.9)	663.6 (± 3.6)	97.8 (± 1.0)
-10	60.6 (± 0.4)	88.0 (± 0.3)	20.9 (± 0.9)	94.0 (± 1.1)	1999.0 (± 8.4)	355.7 (± 1.5)
-20	82.5 (± 0.6)	125.4 (± 0.4)	30.0 (± 1.4)	149.3 (± 1.6)	6523.0 (± 33.4)	1369.0 (± 3.6)
-30	173.3 (± 1.4)	213.6 (± 0.5)	79.0 (± 3.7)	262.0 (± 2.1)	32260 (± 283)	5969 (± 13.1)

Table 2. The temperate-dependent impedance parameters obtained by a fitting with the equivalent circuit (elemental sulfur)

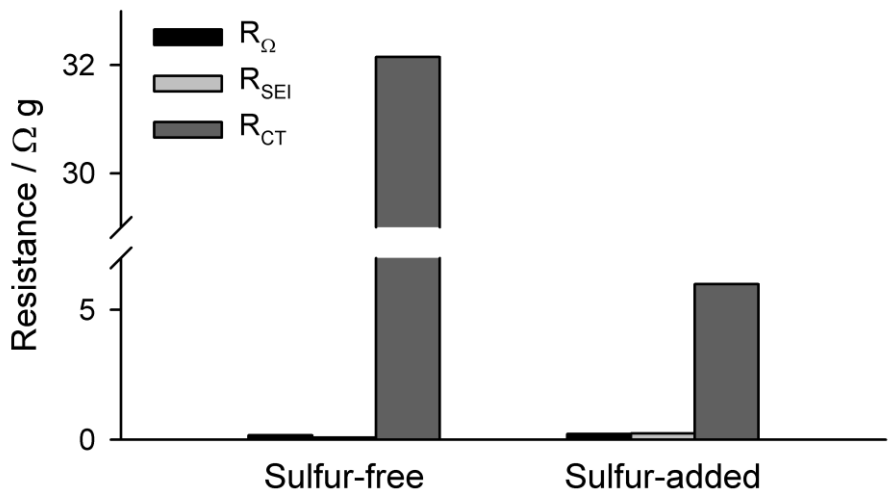

Fig. 23. Comparison between resistance values obtained by a fitting with the equivalent circuit for the sulfur-free and the sulfur-added graphite electrode at -30°C.

the film properties (chemical composition, thickness and so on) are somewhat different to those derived from the background electrolyte. Second, the increase of R_{CT} with a decrease in working temperature is less significant for the sulfur-added electrode; it is about one-fifths of that observed in the sulfur-free electrode at -30°C (Table 2). It can thus be inferred that the smaller R_{CT} is the main reason for the less significant cell polarization at low temperatures for the sulfur-added electrode. It is likely that the sluggish charge transfer reaction at low temperatures is relieved due to the presence of sulfur-enriched surface film.

The charge transfer resistance values have been fitted to the Arrhenius type equation in Fig. 24 by assuming that R_{CT} is a simple thermally activated process [7,90-92],

$$\frac{1}{R_{CT}} = A_0 e^{-E_a/RT}$$

where A_0, R and E_a are a pre-exponential factor, the gas constant and the activation energy. The activation energies are 67.8 kJ mol^{-1} and 62.3 kJ mol^{-1} for the sulfur-free and the sulfur-added graphite, which are consistent with those reported by previous researchers [7,90-92]. The value of activation energy is correlated with graphite/electrolyte interface with the solvent composition and the concentration and type of electrolyte salts as well as with the chemistry of the SEI film [93]. The lower value of the activation energies for the sulfur-added graphite indicates a positive role of the sulfur-containing film in decreasing the energy barrier for the

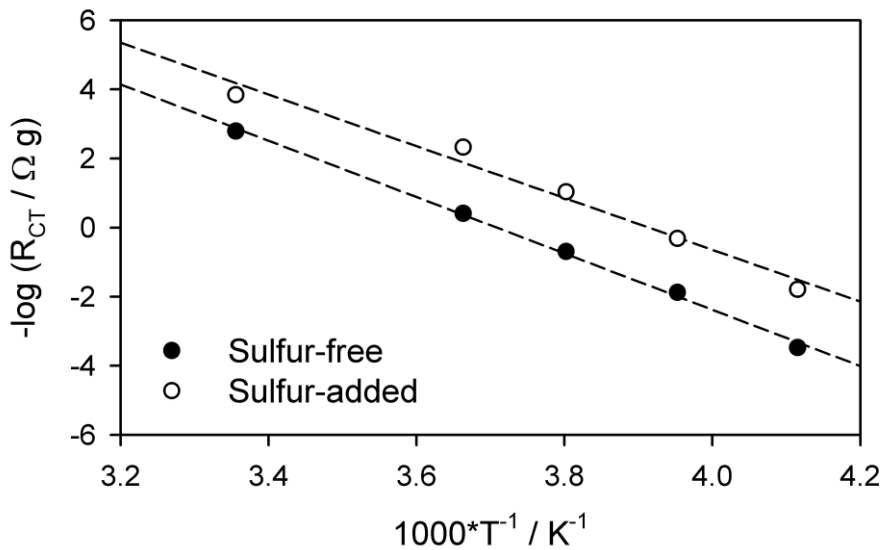

Fig. 24. Arrhenius plots of the charge transfer resistance values obtained by a fitting with the equivalent circuit.

lithium insertion reaction to the graphite structure, and supports the lower charge transfer resistances.

4.2. Allyl sulfide additive for electrolyte

4.2.1. Film-forming mechanism

4.2.1.1. Pre-formed film at OCV

After being fabricated, a Li/graphite cell needs rest time for electrolyte to permeate into the graphite electrodes. During this process, the OCV (open circuit voltage) of the cells alter until the cells reach to the equilibrium state, implying electrochemical environment around the graphite electrode is changed. Fig. 25 presents the initial cell potential (OCV) of Li/graphite cells, after 12 hr rest period. Compared to the control cell with the AS-free electrolyte, adding AS lowers the initial potential of cells after the rest period. The OCV of the AS-added cell is inversely related with the amount of AS added to the background electrolyte, so the cell with 10 wt. % of AS shows 0.5 V (*vs.* Li/Li^+) lower initial potential. It should be noted here that the OCV decrease is a signature of a transfer of Li ions and the equivalent amount of electrons from the electrolyte to the graphite electrode at the interface during the rest period. In this system, by inference, AS additive can be considered to supply electrons to the graphite, suggesting that AS is oxidized on the graphite surface.

The effect of AS additive on the early surface film on the graphite electrode was further studied by FE-SEM (Fig. 26). There is no trace of surface film before it is soaked in the electrolyte (Fig. 26a); the small particles on the surface are the conducting agents, super P. After being soaked, however, some rock-like precipitates are sparsely deposited on the graphite surface after being soaked in the

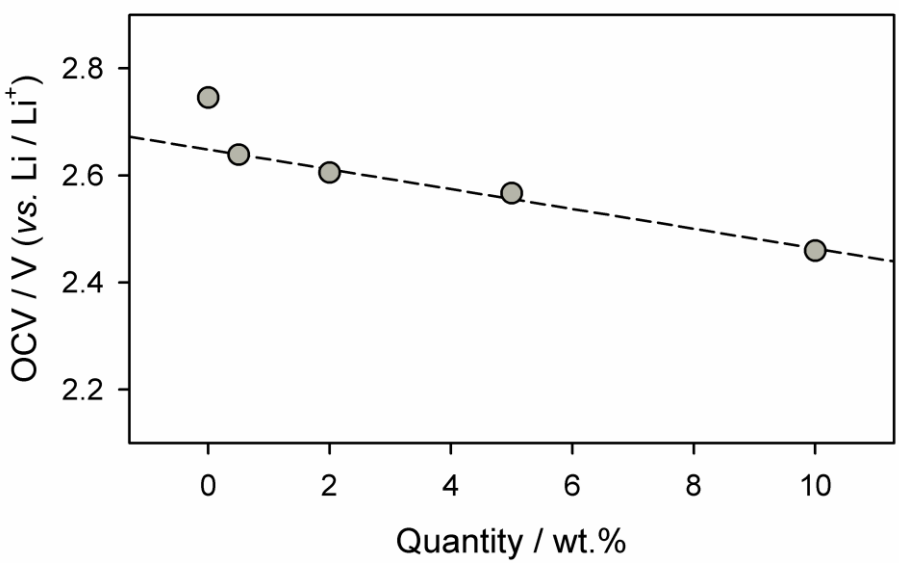

Fig. 25. The initial cell potentials (open circuit voltage) after 12 hr rest period *vs.* the quantity of allyl sulfide additive in the electrolyte.

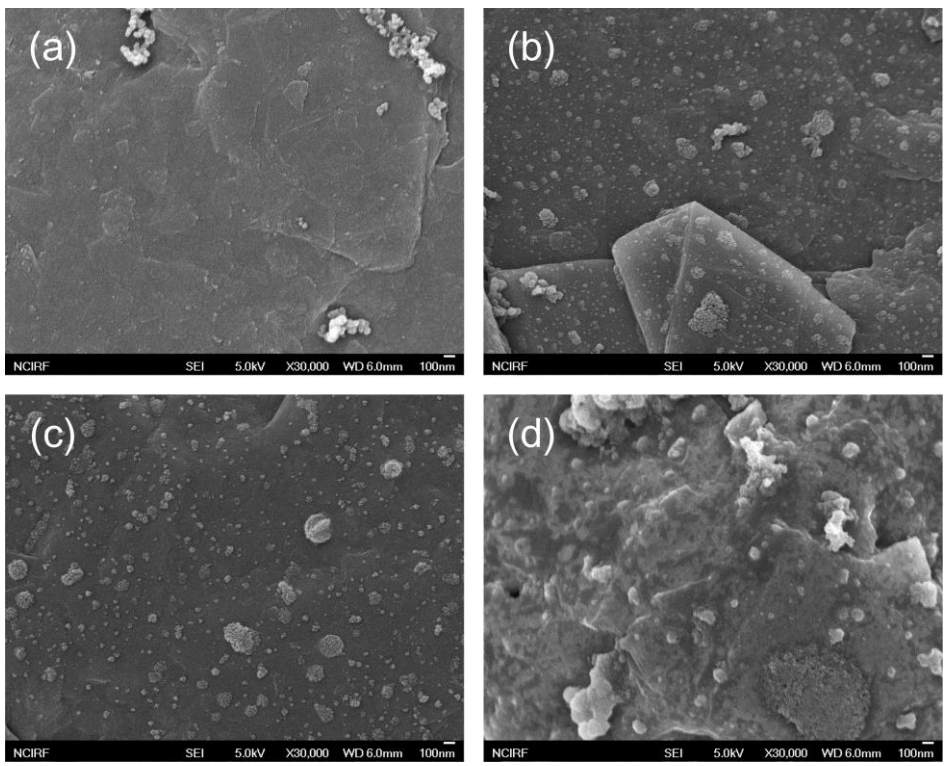

Fig. 26. FE-SEM images of graphite electrode surface obtained (a) before cycling (pristine graphite), (b) after 12 hr being soaked in the background electrolyte, (c) in 2 wt. % AS-added electrolyte, and (d) in 10 wt. % AS-added electrolyte.

AS-free electrolyte or 2 wt. % of AS-added electrolyte (Fig. 26b and c). When the excess AS (10 wt. %, Fig. 26d) was added, a thick surface film is fully covered on the surface, implying that AS contributes to the early film-forming process. From these results, it can be concluded that the AS additive is spontaneously oxidized and generates the pre-formed film on the graphite electrode before the 1st lithiation.

To examine the chemical composition of pre-formed with AS additive on the graphite electrode in rest period, X-ray photoelectron spectroscopy (XPS) analysis is done, as shown in Fig. 27. When compared with the background electrolyte, AS additive make the film contacting sulfur compounds on the graphite electrode spontaneously. S 2p spectrum of the AS-added graphite shows only one peak region around 164 eV, which is attributed to sulfide (-C-S-C-), disulfide (-S-S-) bonds, or elemental sulfur (S_8). As the other sulfur compounds are not appeared in XPS analysis, the oxidation products from AS additive can be considered to disulfide species (oxidation state = -1) or elemental sulfur (oxidation state = 0). To narrow down candidates, the OCV behavior of Li/graphite cells which include various additives are examined in Fig. 28. When the additives containing sulfide bond in them are added to the electrolyte, the initial potential of the cells after 12 hr rest period decreases while disulfide additives maintain comparable OCV value with the background electrolyte. This tendency implies that disulfide species are not oxidized at the OCV of graphite (~2.7 V *vs.* Li/Li^+), therefore, the sulfide species can be oxidized to disulfide but not to elemental sulfur. From these results, the disulfide species are considered as a strong candidate for the oxidation product of AS additive during rest period.

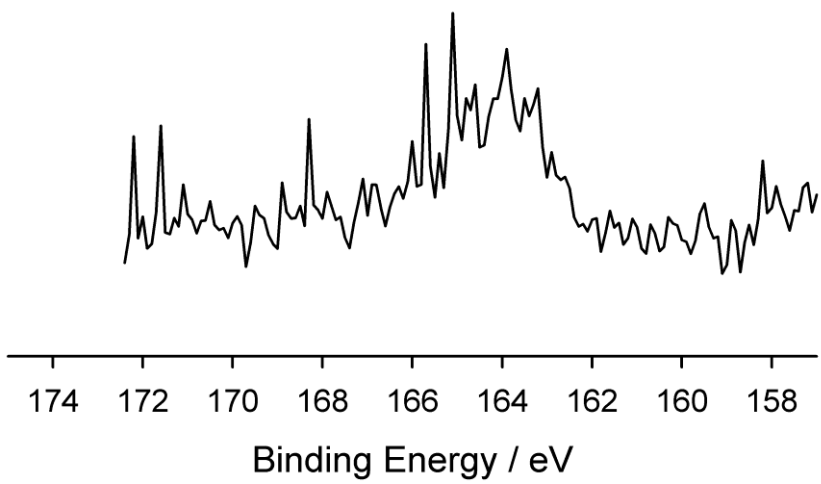

Fig. 27. S 2p XPS spectrum of the AS-added graphite electrode after 12 hr rest period.

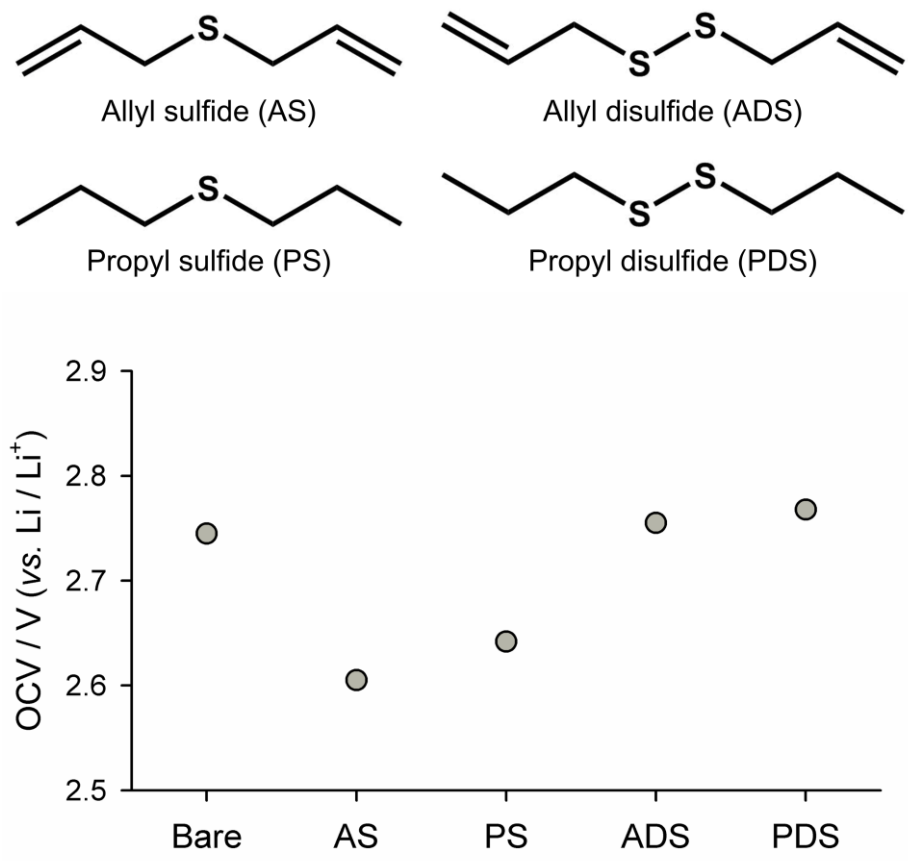

Fig. 28. The initial cell potentials (open circuit voltage) of Li/graphite cells after 12 hr rest period with various electrolyte additive.

The dQ/dV plots of the 1st lithiation step of the AS-free and the AS-added graphite electrodes are compared in Fig. 29. There appears a distinctive peak at 1.55 V (*vs.* Li/Li^+) on the dQ/dV plot obtained from the AS-added graphite electrode (Fig. 29b). This peak indicates the pre-formed film derived from allyl sulfide additive is reduced in the 1st lithiation step before other electrolyte components are reduced (the reduction peak around 0.7 V *vs.* Li/Li^+ in Fig. 29a). Like the sulfur-added graphite, the reduction peak of the background electrolyte of the AS-added graphite electrode appears at 0.68 V, which is about 0.1 V higher than the AS-free one. This can be interpreted as an effect of the pre-formed film which reduce the resistance of the electrode.

4.2.1.2. Form of sulfur compounds during pre-cycling

To understand of the mechanism of film formation with the allyl sulfide additive, the change in chemical composition of the surface film was analyzed with XPS. The S2p spectra in 1st cycle are shown in Fig. 30. After 12 hr rest period, allyl sulfide additive forms a surface film containing sulfide or disulfide species [76,77] as described above. This film is reduced at 1st lithiation and participates in SEI-forming process. The AS-derived film is found in the deeper region (after 600 s etching) of the film, similar with the case of elemental sulfur additive, while the outer region is covered by the sulfur-free film from background electrolyte. The AS-derived film in this step contains Li_2S (161.0 eV) [76,77]. Notably, the sulfur compounds include oxygen species in them, like thiocarbonates, are not present in the AS-derived film. From this, it can be inferred that allyl sulfide additive does not

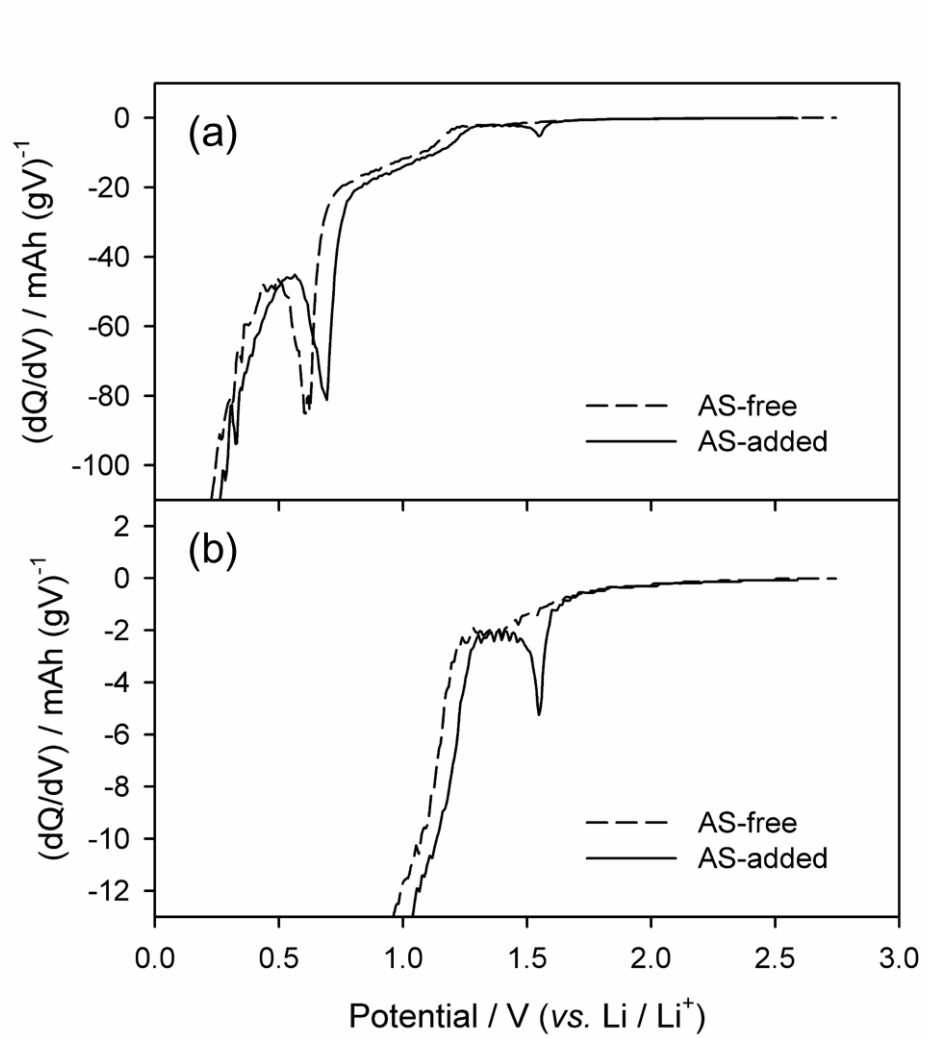

Fig. 29. Differential capacity plot (dQ/dV) for the 1st lithiation step at 25°C: (a) full-range; (b) magnification of dQ/dV plot (reduction related with allyl sulfide additive).

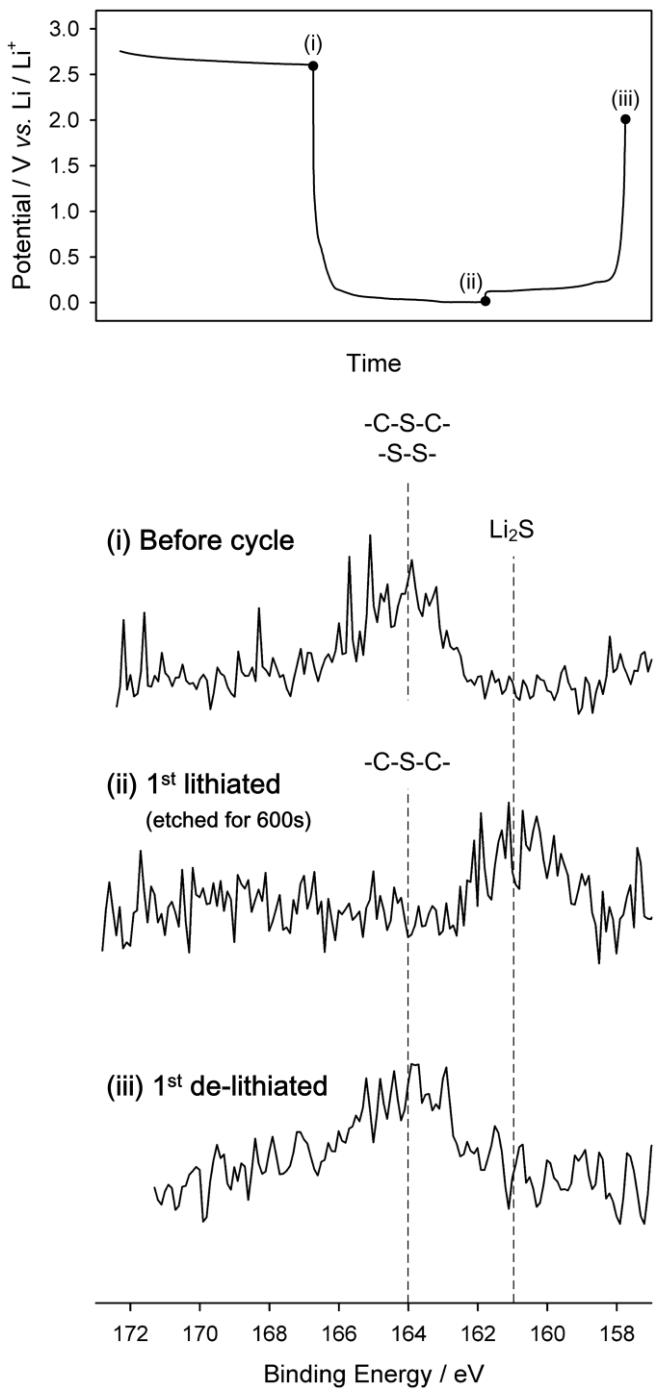

Fig. 30. S 2p XPS spectra obtained from the AS-added graphite electrode during pre-cycling (1st cycle).

react with electrolyte components, but only with graphite electrode. After 1st de-lithation, the topmost of the film consists of sulfide (-C-S-C-) or disulfide (-S-S-) species.

4.2.1.3. Chemical aspects of the SEI chemistry

The composition of the fully-formed SEI after pre-cycling was analyzed using XPS. The S 2p spectra and the chemical composition through the depth are shown in Fig. 31. After the stable SEI is formed, the AS-derived film is found in the deeper region (after 120 s etching and more) of the SEI, and the outer region is covered by the film derived from background electrolyte. This implies the pre-formed film from allyl sulfide additive in the rest period is reduced in pre-cycling and develops the inner region of the SEI film, which consists of mostly sulfide (-C-S-C-) or disulfide (-C-S-S-C-) species. The two surface films show similar composition at topmost region (Fig. 31), illustrating that the film from the background electrolyte covers the AS-derived film. The AS-derived film, near the graphite surface, is plenty of C-species and has less F-species in it. It implies that the pre-formed film in rest period covers the bare graphite and prevents $LiPF_6$ salt decomposition on the graphite surface, thus also prevents generation of inorganic F-species. The morphology of SEI films of two electrodes are quite similar, as shown is Fig. 32.

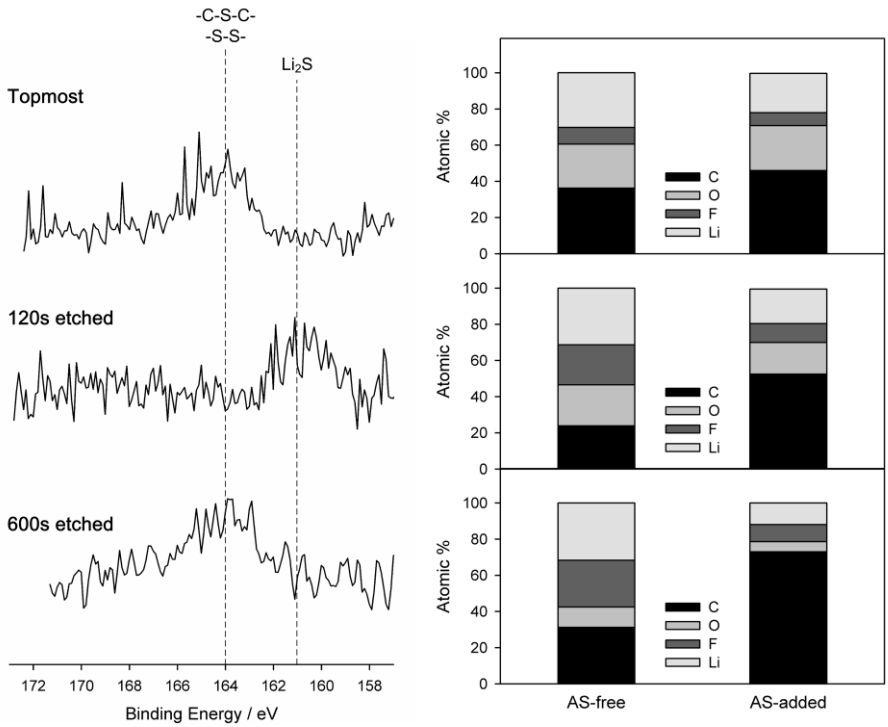

Fig. 31. S 2p spectra and the variation of chemical composition of film depth. The results were obtained by fitting the depth-profiling XPS data. The measurement was made after 5th de-lithiation.

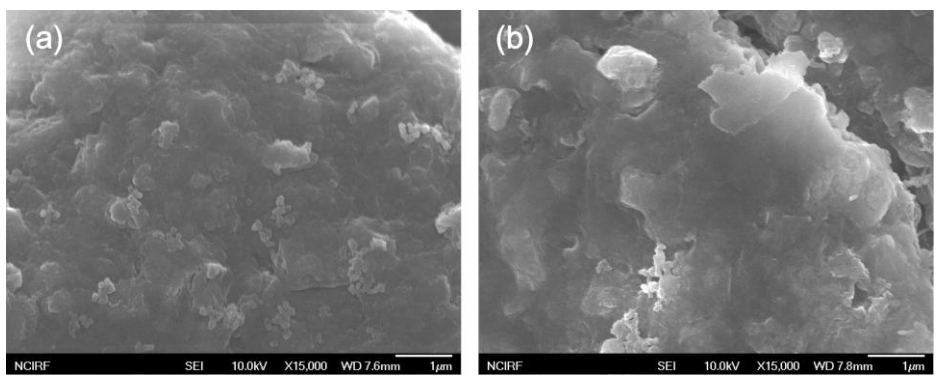

Fig. 32. FE-SEM image of (a) the AS-free and (b) the AS-added graphite electrode after pre-cycled.

4.2.2. Low-temperature performance

4.2.2.1. Lithiation/de-lithiation performance

Fig. 33 compares lithiation/de-lithiation behaviors for two Li/graphite cells which contain the AS-added and AS-free electrolyte. At 25^{o}C, two cells exhibit a similar reversible capacity (~365 mAh g^{-1}) and the Coulombic efficiency (~99%), indicating that AS does not have an adverse effect on the performance of graphite in general temperature condition. As the temperature decrease (-10^{o}C and -30^{o}C, Fig. 33), the available capacity of both cells decreases because of large overpotential applied to the electrodes, while the AS-added cell is superior in the reversible capacity to the AS-free cell. The capacity difference between the two cells becomes greater as the temperature drops, therefore the reversible capacity of the AS-added cell is almost twice as large as the AS-free cell. It is worth noticing that the Coulombic efficiency of the two cells is similar even at -30^{o}C, suggesting that inserted lithium in the graphite structure easily moves out regardless of the temperature [7,94]. Since the major lithiation process occurs close to the cutoff potential (0.005 vs. Li/Li+), the lithiation capacity of graphite is sensitive to cell polarization. Therefore, a slight difference in cell polarization causes a significant difference in the lithiation capacity, thus the de-lithiation capacity and further the reversible capacity.

4.2.2.2. Li plating (pulse test)

In Fig. 34, the voltage difference from de-lithiation ($\Delta V_D = | V_{1D} - V_{2D}|$) and

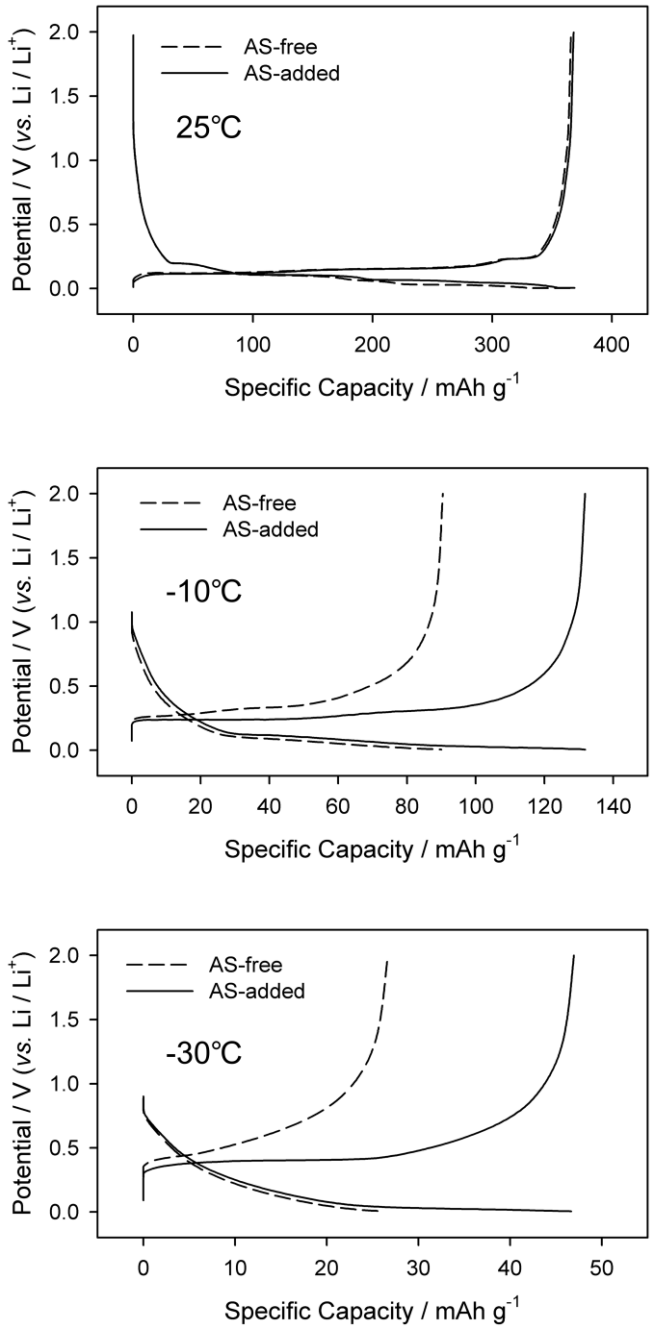

Fig. 33. Comparison of the reversible capacity for two Li/graphite cells, into which the AS-added and AS-free graphite electrode were loaded separately. The cells were pre-cycled five times at 25°C before the test. Voltage cutoff = 0.005~2.0 V. Current density = 74.4 mA g^{-1} (0.2 C-rate) at 25°C, -10°C and 18.6 mA g^{-1} (0.05 C-rate) at -30°C.

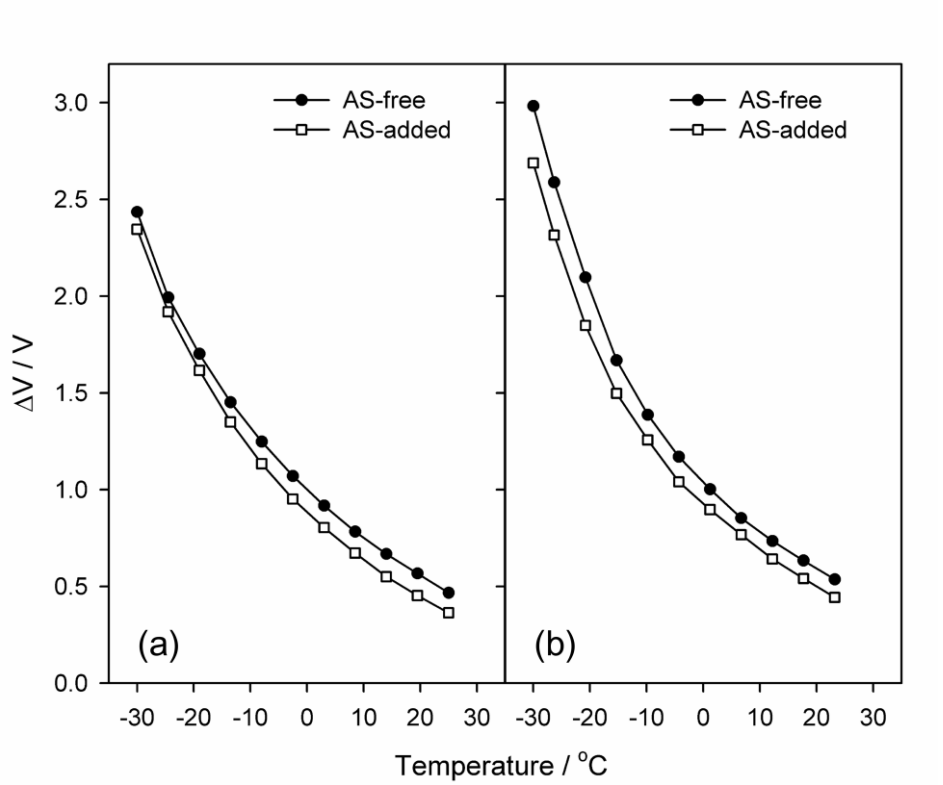

Fig. 34. A comparison of voltage difference ($\Delta V = |V_1 - V_2|$) for the (a) de-lithiation (ΔV_D) and (b) lithiation current pulse (ΔV_L) as a function of temperature (25~-30°C) at a fixed pulse height (10 C-rate).

lithiation ($\Delta V_L = |V_{1L} - V_{2L}|$) pulse is plotted as a function of temperature. In both cases, the voltage difference of the AS-added cell is smaller, indicating that the cell overpotential of the AS-added cell is smaller than that of the AS-free. The difference in lithiation pulse is higher than in de-litiation, reconfirming that lithiation into graphite is more difficult. During the pulse test, Li^+ intercalation/de-intercalation is made within a narrow range of SOC (50 ± 2.8 %).

Fig. 35 shows the voltage transients obtained from two cells at the 6 hr rest period after the lithiation pulse (10 C-rate). At relatively high temperatures (≥ 12.2°C), the potential of the AS-free cell immediately restores back to the initial equilibrium value (~0.12 V *vs.* Li/Li^+). A similar voltage restoration is observed at lower temperatures (≤ -9.8°C), but after giving rise to a voltage plateau (Fig. 35a). This voltage plateau represents the mixed potential and thus a signature for lithium plating. Namely, the plated metallic lithium on the graphite electrode tends to be oxidized ($yLi \rightarrow yLi^+ + ye$) during the rest period, and the graphite electrode is reduced ($Li_xC_6 + yLi^+ + ye \rightarrow Li_{x+y}C_6$) by taking the released lithium ions (yLi^+) and electrons (ye). A local galvanic cell forms by these coupled electrochemical reactions, and the graphite electrode now shows a mixed potential that is pinned at the middle of two electrode potentials [95]. With an increase in lithium plating, the mixed potential appears at a lower value (closer to the lithium plating potential) and its duration in the relaxation profiles is longer. All these features are clearly seen in Fig. 35a. That is, the profile obtained at the lowest temperature (-30°C), under which condition the largest amount of lithium plating is expected, exhibits the lowest mixed potential that prevails for the longest period of time. In case of the AS-added cell (Fig. 35b), otherwise, the mixed potential is not clearly appeared

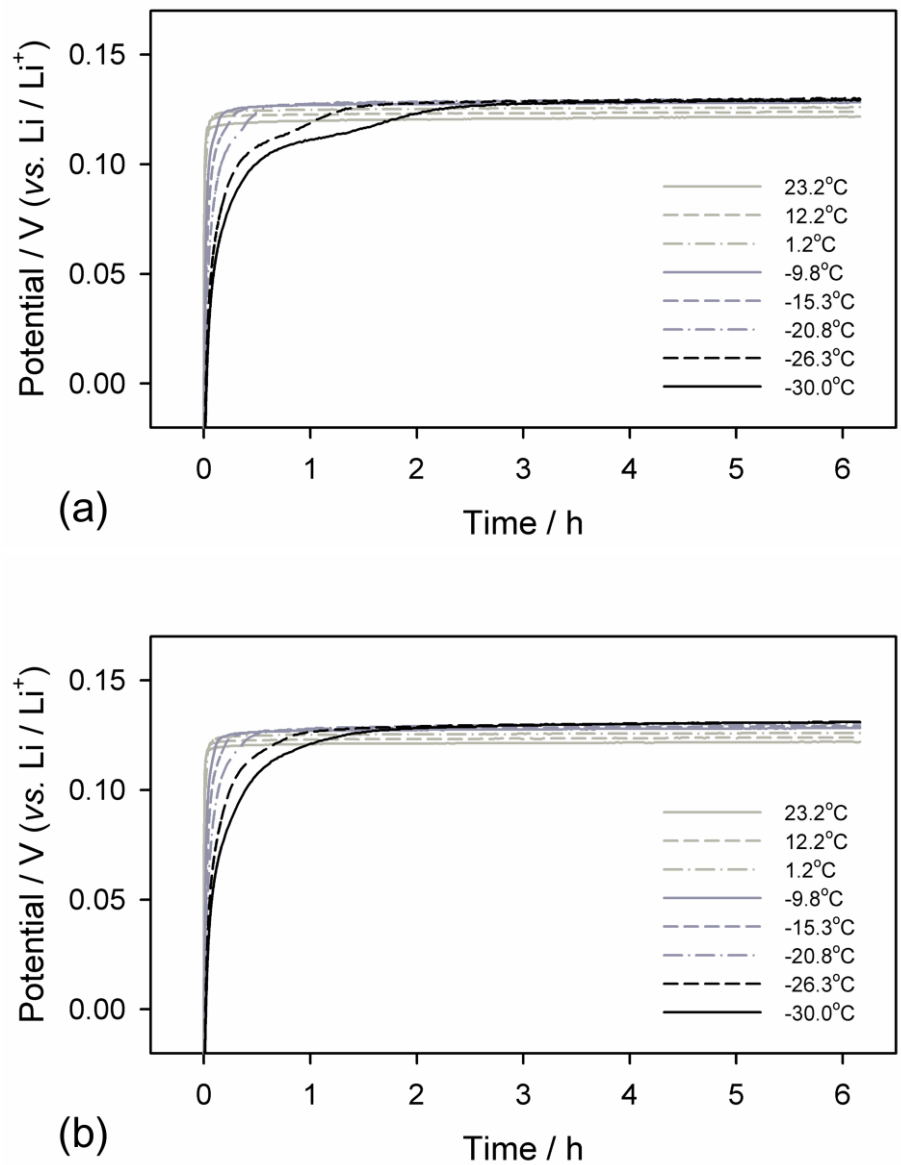

Fig. 35. The voltage relaxation profiles of (a) the sulfur-free graphite electrode and (b) the sulfur-added one during 6 hr rest period after a lithiation pulse (10 C-rate) at different temperatures. The temperature at the beginning of lithiation pulse is indicated in the inset.

even at -30°C, indicating that lithium plating is suppressed in low-temperature conditions.

4.2.2.3. Electrochemical impedance spectroscopy (EIS)

The cell polarization in Li/graphite cells were examined using impedance analysis. Fig. 36 shows the Nyquist plots and Table 3 lists the impedance parameters obtained by fitting the spectra with a Voigt-type equivalent circuit [86-88], as described in previous section. As is listed Table 3, all the resistance values increase with a decrease in the working temperature. Especially, the increase of R_{CT} (charge transfer resistance) is significant in both cells, implying this resistance component accounts for the increase in cell resistance. As shown in Fig. 37, the charge transfer resistance is a main component at -30°C.

When allyl sulfide additive is added to the electrolyte, the resistance related with Li^+ transport through surface film (R_{SEI}) increases slightly, implying that the film properties (chemical composition, thickness and so on) are somewhat different to those derived from the background electrolyte. The increase of R_{CT}, whereas, with a decrease in working temperature is less severe for the AS-added cell; it is about half of that observed in the AS-free cell at -30°C. As inferred above, the smaller R_{CT} is suggested to be a main reason for the less significant cell polarization at low temperatures for the AS-added graphite cell. It can be reconfirmed that sulfur-enriched surface film relieves the sluggish charge transfer reaction at low-temperatures.

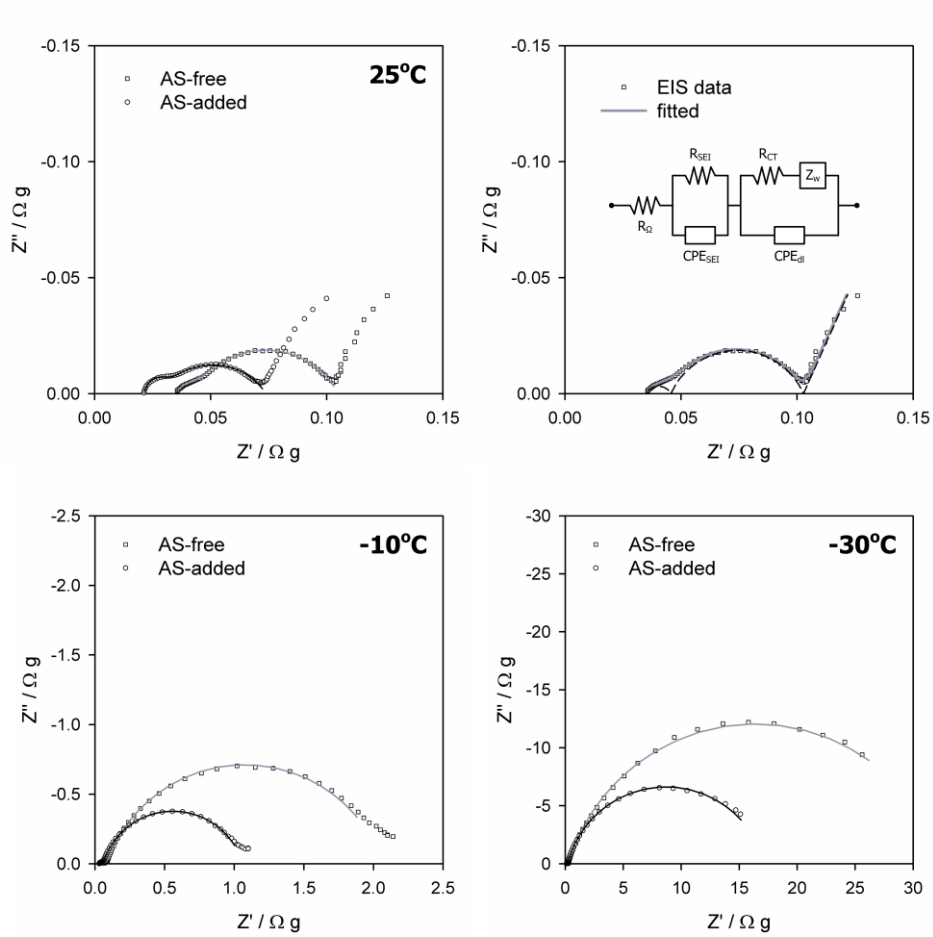

Fig. 36. The Nyquist plots obtained from the symmetric cells as a function of temperature. The typical fitting result performed with the equivalent circuit is represented at the upper-right corner.

	R_{Ω} (mΩ g)		R_{SEI} (mΩ g)		R_{CT} (mΩ g)	
Temperature (℃)	**Sulfur-free**	**Sulfur-added**	**Sulfur-free**	**Sulfur-added**	**Sulfur-free**	**Sulfur-added**
25	35.1 (± 0.2)	21.2 (± 0.2)	8.4 (± 0.5)	7.5 (± 1.1)	61.3 (± 0.6)	45.2 (± 0.9)
0	49.2 (± 0.3)	23.7 (± 0.1)	16.4 (± 0.7)	18.5 (± 0.5)	663.6 (± 3.6)	320.0 (± 2.5)
-10	60.6 (± 0.4)	30.4 (± 0.1)	20.9 (± 0.9)	26.2 (± 0.5)	1999.0 (± 8.4)	1004.0 (± 5.1)
-20	82.5 (± 0.6)	44.5 (± 0.1)	30.0 (± 1.4)	44.0 (± 0.5)	6523.0 (± 33.4)	3456.0 (± 12.2)
-30	173.3 (± 1.4)	99.1 (± 0.3)	79.0 (± 3.7)	110.4 (± 1.1)	32260 (± 283)	16620 (± 86)

Table 3. The temperate-dependent impedance parameters obtained by a fitting with the equivalent circuit (allyl sulfide)

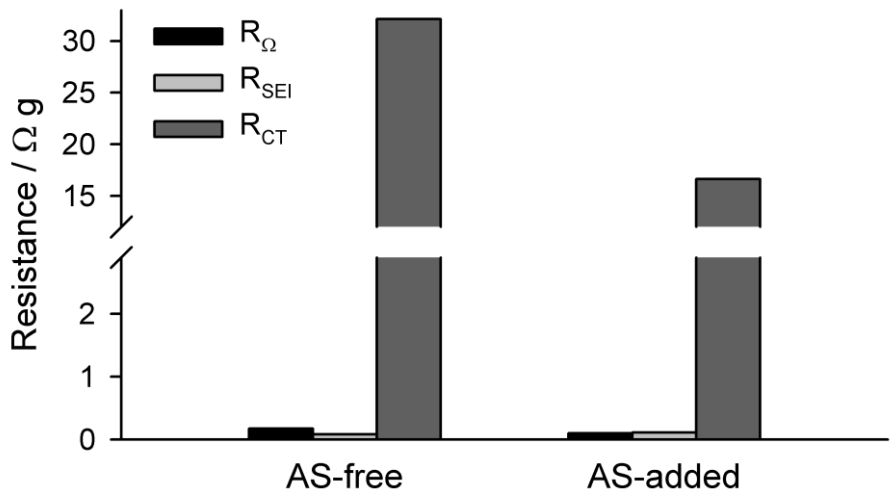

Fig. 37. Comparison between resistance values obtained by a fitting with the equivalent circuit for the AS-free and the AS-added cell at -30°C.

To calculate the activation energy of cells, the charge transfer resistance values have been fitted to the Arrhenius type equation (Fig. 38). The activation energies obtained from the AS-free and the AS added cell are 67.8 kJ and 65.4 mol^{-1}. Like the sulfur added system, the sulfur-containing film is suggested to do a positive role of in decreasing the energy barrier for the lithium insertion reaction to the graphite structure, and supports the lower charge transfer resistances.

Based on results, we propose a mechanism for the film-forming process with allyl sulfide depicted by the schematic in Fig. 39. Schematic illustration for the film-forming process of allyl sulfide additive.. As illustrated, the film-forming process can be divided into two stages: (i) during the rest period, AS additive is spontaneously oxidized and makes the pre-formed surface film on the graphite surface; and (ii) this pre-formed film is developed into the inner layer of SEI during pre-cycling, while the upper surface of the film is covered by the AS-free deposits from the background electrolyte.

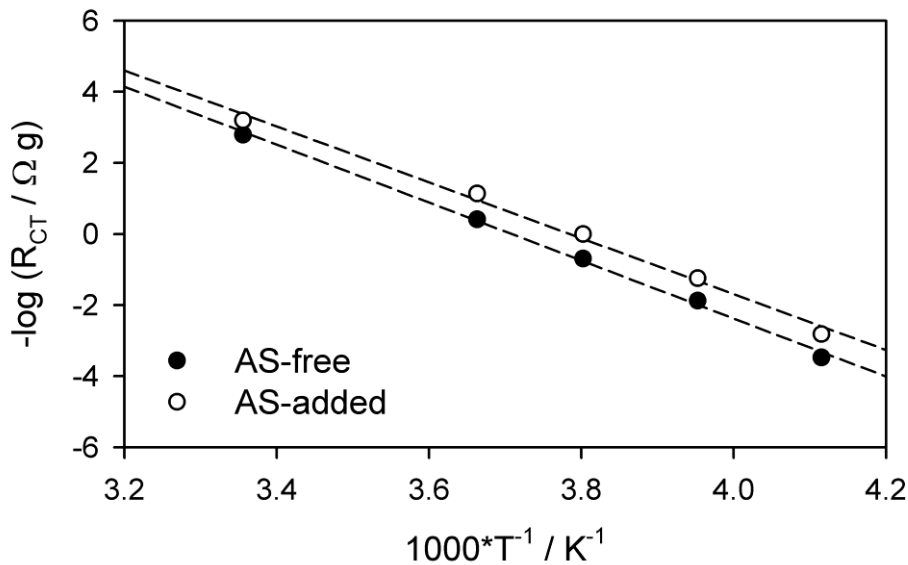

Fig. 38. Arrhenius plots of the charge transfer resistance values obtained by a fitting with the equivalent circuit.

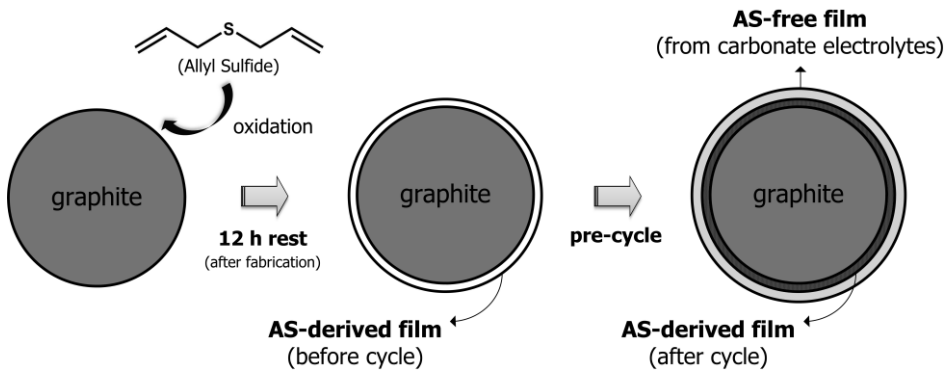

Fig. 39. Schematic illustration for the film-forming process of allyl sulfide additive.

5. CONCLUSION

In summary, the film-forming process with each sulfur-containing additive was investigated, and low-temperature characteristics of consequent surface films were examined. The following are the major findings of the study.

(i) Elemental sulfur generates SEI film through a three-step process. First, sulfur is electrochemically reduced to lithium polysulfide (Li_2S_8) at ~2.0 V (vs. Li/Li^+), which is soluble in the working solvent (carbonate-based ones). Organic thiocarbonates, then, are generated by the chemical reaction between the lithium polysulfide and carbonate solvents. During pre-cycling, these as-generated thiocarbonates are electrochemically decomposed to form the sulfur-containing surface film, which has sulfide (-C-S-C-) and thiocarbonates (-O-CO-S-) bridges and less F-species in it.

(ii) Allyl sulfide generates SEI film through a simpler two-step process. In 12 hr rest period before cycle, allyl sulfide additive is spontaneously oxidized and forms a pre-film on the surface of graphite. During pre-cycling, this pre-formed film is reduced and develops inner film in the SEI layer, which has sulfide (-C-S-C-) bridges and less F-species.

(iii) Elemental sulfur and allyl sulfide enhance the low-temperature performance of the Li/graphite cell in reversible capacity and prevention of Li plating. The surface film derived from sulfur-

containing additives is less resistive at low-temperature; especially, the charge transfer resistance is significantly decreased. This improvement is attributed to two physio-chemical aspects of SEI; (i) more elastic polymer structure due to the presence of sulfur bridges (-C-S-C- and -O-CO-S-), and (ii) decrease of inorganic components which are considered as a reason of high resistance.

(iv) Both additives, elemental sulfur and allyl sulfide, can be used to improve the low-temperature characteristics of graphite. Among these, allyl sulfide is more appropriate for commercial use since elemental sulfur involves side reactions related with the production of thiocarbonates.

REFERENCES

1. J. Fan, *J. Power Sources*, **117**, 170 (2003).

2. S. S. Zhang, K. Xu and T. R. Jow, *Electrochim. Acta*, **49**, 1057 (2004).

3. DOE, *Energy storage R&D annual progress report*, **81** (2011).

4. M. C. Smart, B. V. Ratnakumar and S. Surampudi, *J. Electrochem. Soc.*, **149**, A361 (2002).

5. F. Nobili, S. Dsoke, T. Mecozzi and R. Marassi, *Electrochim. Acta*, **51**, 536 (2005).

6. J. Li, C. F. Yuan, Z. H. Guo, Z. A. Zhang, Y. Q. Lai and J. Liu, *Electrochim. Acta*, **59**, 69 (2012).

7. M. Mancini, F. Nobili, S. Dsoke, F. D'Amico, R. Tossici, F. Croce and R. Marassi, *J. Power Sources*, **190**, 141 (2009).

8. M. Marinaro, M. Mancini, F. Nobili, R. Tossici, L. Damen and R. Marassi, *J. Power Sources*, **222**, 66 (2013).

9. D. Aurbach, B. Markovsky, I. Weissman, E. Levi and Y. Ein-Eli, *Electrochim. Acta*, **45**, 67 (1999).

10. P. Verma, P. Maire and P. Novak, *Electrochim. Acta*, **55**, 6332 (2010).

11. P. Lu, C. Li, E. W. Schneider and S. J. Harris, *The Journal of Physical Chemistry C*, **118**, 896 (2014).

12. T. Kawaguchi, K. Shimada, T. Ichitsubo, S. Yagi and E. Matsubara, *J. Power Sources*, **271**, 431 (2014).

13. K. Xu and A. von Cresce, *J. Mater. Chem.*, **21**, 9849 (2011).

14. T. Ohtomo, A. Hayashi, M. Tatsumisago and K. Kawamoto, *J. Solid State Electrochem.*, **17**, 2551 (2013).

15. J. E. Trevey, J. R. Gilsdorf, S. W. Miller and S.-H. Lee, *Solid State Ionics*,

214, 25 (2012).

16. K. Minami, F. Mizuno, A. Hayashi and M. Tatsumisago, *J. Non-Cryst. Solids*, **354**, 370 (2008).

17. T. Minami, A. Hayashi and M. Tatsumisago, *Solid State Ionics*, **177**, 2715 (2006).

18. R. Kanno and M. Murayama *J. Electrochem. Soc.*, **148**, A742 (2001).

19. Y. Ein-Eli, S. R.thomas and V. R. Koch, *J. Electrochem. Soc.*, **143**, L195 (1996).

20. Y. Ein-Eli, *J. Electroanal. Chem.*, **531**, 95 (2002).

21. J. O. Besenhard, M. W. Wagner, M. Winter, A. D. Jannakoudakis, P. D. Jannakoudakis and E. Theodoridou, *J. Power Sources*, **44**, 413 (1993).

22. M. W. Wagner, C. Liebenow and J. O. Besenhard, *J. Power Sources*, **68**, 328 (1997).

23. M. Winter, W. K. Appel, B. Evers, T. Hodal, K. C. Moller, I. Schneider, M. Wachtler, M. R. Wagner, G. H. Wrodnigg and J. O. Besenhard, *Monatsh. Chem.*, **132**, 473 (2001).

24. G. H. Wrodnigg, T. M. Wrodnigg, J. O. Besenhard and M. Winter, *Electrochem. Commun.*, **1**, 148 (1999).

25. M. S. Whittingham, *Science*, **192**, 1126 (1976).

26. J. O. Besenhard, *Carbon*, **14**, 111 (1976).

27. J. O. Besenhard and H. P. Fritz, *Journal of Electroanalytical Chemistry and Interfacial Electrochemistry*, **53**, 329 (1974).

28. J. O. Besenhard and R. Schöllhorn, *J. Power Sources*, **1**, 267 (1976).

29. R. Schöllhorn, R. Kuhlmann and J. O. Besenhard, *Mater. Res. Bull.*, **11**, 83 (1976).

30. J. O. Besenhard and G. Eichinger, *Journal of Electroanalytical Chemistry*

and Interfacial Electrochemistry, **68**, 1 (1976).

31. G. Eichinger and J. O. Besenhard, *Journal of Electroanalytical Chemistry and Interfacial Electrochemistry*, **72**, 1 (1976).

32. K. Mizushima, P. C. Jones, P. J. Wiseman and J. B. Goodenough, *Mater. Res. Bull.*, **15**, 783 (1980).

33. R. Yazami and P. Touzain, *J. Power Sources*, **9**, 365 (1983).

34. D. Aurbach, B. Markovsky, A. Shechter, Y. EinEli and H. Cohen, *J. Electrochem. Soc.*, **143**, 3809 (1996).

35. K. Kanamura, H. Takezawa, S. Shiraishi and Z. i. Takehara, *J. Electrochem. Soc.*, **144**, 1900 (1997).

36. D. Aurbach and Y. Cohen, *J. Electrochem. Soc.*, **143**, 3525 (1996).

37. Y. S. Cohen, Y. Cohen and D. Aurbach, *The Journal of Physical Chemistry B*, **104**, 12282 (2000).

38. D. Aurbach, E. Zinigrad, Y. Cohen and H. Teller, *Solid State Ionics*, **148**, 405 (2002).

39. G. Zheng, S. W. Lee, Z. Liang, H.-W. Lee, K. Yan, H. Yao, H. Wang, W. Li, S. Chu and Y. Cui, *Nat Nano*, **9**, 618 (2014).

40. T. Ohzuku, Y. Iwakoshi and K. Sawai, *J. Electrochem. Soc.*, **140**, 2490 (1993).

41. J. R. Dahn, W. Xing and Y. Gao, *Carbon*, **35**, 825 (1997).

42. R. Alcántara, J. M. Jiménez Mateos and J. L. Tirado *J. Electrochem. Soc.*, **149**, A201 (2002).

43. J. Wang, I. D. Raistrick and R. A. Huggins, *J. Electrochem. Soc.*, **133**, 457 (1986).

44. M. Winter and J. O. Besenhard, *Electrochim. Acta*, **45**, 31 (1999).

45. A. N. Dey, *J. Electrochem. Soc.*, **118**, 1547 (1971).

46. C. J. Wen and R. A. Huggins, *J. Solid State Chem.*, **37**, 271 (1981).

47. J. H. Ryu, J. W. Kim, Y.-E. Sung and S. M. Oh, *Electrochem. Solid-State Lett.*, **7**, A306 (2004).

48. C. J. Wen and R. A. Huggins, *J. Electrochem. Soc.*, **128**, 1181 (1981).

49. U. Kasavajjula, C. Wang and A. J. Appleby, *J. Power Sources*, **163**, 1003 (2007).

50. G. Taillades, N. Benjelloun, J. Sarradin and M. Ribes, *Solid State Ionics*, **152–153**, 119 (2002).

51. J. N. Reimers and J. R. Dahn, *J. Electrochem. Soc.*, **139**, 2091 (1992).

52. J. Cho, Y. J. Kim, T.-J. Kim and B. Park, *Angew. Chem. Int. Ed.*, **40**, 3367 (2001).

53. R. J. Gummow, A. de Kock and M. M. Thackeray, *Solid State Ionics*, **69**, 59 (1994).

54. D. H. Jang and S. M. Oh, *J. Electrochem. Soc.*, **144**, 3342 (1997).

55. K. Xu, *Chem. Rev.*, **114**, 11503 (2014).

56. R. Fong, U. von Sacken and J. R. Dahn, *J. Electrochem. Soc.*, **137**, 2009 (1990).

57. E. Peled, D. Golodnitsky, C. Menachem and D. Bar-Tow, *J. Electrochem. Soc.*, **145**, 3482 (1998).

58. M. Lu, H. Cheng and Y. Yang, *Electrochim. Acta*, **53**, 3539 (2008).

59. O. Yariv, D. Hirshberg, E. Zinigrad, A. Meitav, D. Aurbach, M. Jiang and B. R. Powell, *J. Electrochem. Soc.*, **161**, A1422 (2014).

60. L. X. Liao, X. Q. Cheng, Y. L. Ma, P. J. Zuo, W. Fang, G. P. Yin and Y. Z. Gao, *Electrochim. Acta*, **87**, 466 (2013).

61. L. X. Liao, T. Fang, X. G. Zhou, Y. Z. Gao, X. Q. Cheng, L. L. Zhang and G. P. Yin, *Solid State Ionics*, **254**, 27 (2014).

62. B. X. Liu, B. Li and S. Y. Guan, *Electrochem Solid St*, **15**, A77 (2012).

63. S. S. Zhang, *J. Power Sources*, **162**, 1379 (2006).

64. C. H. Chen, J. Liu and K. Amine, *J. Power Sources*, **96**, 321 (2001).

65. R. Petibon, C. P. Aiken, N. N. Sinha, J. C. Burns, H. Ye, C. M. VanElzen, G. Jain, S. Trussler and J. R. Dahn, *J. Electrochem. Soc.*, **160**, A117 (2013).

66. R. D. Rauh, F. S. Shuker, J. M. Marston and S. B. Brummer, *J. Inorg. Nucl. Chem.*, **39**, 1761 (1977).

67. K. Tezuka, W. C. Sheets, R. Kurihara, Y. J. Shan, H. Imoto, T. J. Marks and K. R. Poeppelmeier, *Solid State Sci.*, **9**, 95 (2007).

68. R. Blachnik and A. Müller, *Thermochim. Acta*, **361**, 31 (2000).

69. J. S. Chung and H. J. Sohn, *J. Power Sources*, **108**, 226 (2002).

70. B. Jache, B. Mogwitz, F. Klein and P. Adelhelm, *J. Power Sources*, **247**, 703 (2014).

71. C.-H. Lai, K.-W. Huang, J.-H. Cheng, C.-Y. Lee, B.-J. Hwang and L.-J. Chen, *J. Mater. Chem.*, **20**, 6638 (2010).

72. Y. X. Yin, S. Xin, Y. G. Guo and L. J. Wan, *Angew. Chem. Int. Ed.*, **52**, 13186 (2013).

73. J. Zheng, M. Gu, C. Wang, P. Zuo, P. K. Koech, J.-G. Zhang, J. Liu and J. Xiao, *J. Electrochem. Soc.*, **160**, A1992 (2013).

74. T. Yim, M.-S. Park, J.-S. Yu, K. J. Kim, K. Y. Im, J.-H. Kim, G. Jeong, Y. N. Jo, S.-G. Woo, K. S. Kang, I. Lee and Y.-J. Kim, *Electrochim. Acta*, **107**, 454 (2013).

75. J. Gao, M. A. Lowe, Y. Kiya and H. D. Abruña, *Journal of Physical Chemistry C*, **115**, 25132 (2011).

76. H. Ota, T. Akai, H. Namita, S. Yamaguchi and M. Nomura, *J. Power Sources*, **119–121**, 567 (2003).

77. C. C. Chang, S. H. Hsu, Y. F. Jung and C. H. Yang, *J. Power Sources*, **196**, 9605 (2011).

78. S. Slavin, A. H. Soeriyadi, L. Voorhaar, M. R. Whittaker, C. R. Becer, C. Boyer, T. P. Davis and D. M. Haddleton, *Soft Matter*, **8**, 118 (2012).

79. R. Dedryvere, H. Martinez, S. Leroy, D. Lemordant, F. Bonhomme, P. Biensan and D. Gonbeau, *J. Power Sources*, **174**, 462 (2007).

80. D. Aurbach, I. Weissman, A. Schechter and H. Cohen, *Langmuir*, **12**, 3991 (1996).

81. A. M. Andersson and K. Edstrom, *J. Electrochem. Soc.*, **148**, A1100 (2001).

82. R. Dedryvère, S. Laruelle, S. Grugeon, L. Gireaud, J.-M. Tarascon and D. Gonbeau, *J. Electrochem. Soc.*, **152**, A689 (2005).

83. L. El Ouatani, R. Dedryvere, C. Siret, P. Biensan, S. Reynaud, P. Iratcabal and D. Gonbeau, *J. Electrochem. Soc.*, **156**, A103 (2009).

84. D. Aurbach, A. Zaban, Y. Ein-Eli, I. Weissman, O. Chusid, B. Markovsky, M. Levi, E. Levi, A. Schechter and E. Granot, *J. Power Sources*, **68**, 91 (1997).

85. K. C. Hogstrom, S. Malmgren, M. Hahlin, H. Rensmo, F. Thebault, P. Johansson and K. Edstrom, *Journal of Physical Chemistry C*, **117**, 23476 (2013).

86. B. Markovsky, M. D. Levi and D. Aurbach, *Electrochim. Acta*, **43**, 2287 (1998).

87. Y. S. Jung, P. Lu, A. S. Cavanagh, C. Ban, G. H. Kim, S. H. Lee, S. M. George, S. J. Harris and A. C. Dillon, *Advanced Energy Materials*, **3**, 213 (2013).

88. A. Zaban, E. Zinigrad and D. Aurbach, *J. Phys. Chem.*, **100**, 3089 (1996).

89. D. Aurbach, M. D. Levi and E. Levi, *Solid State Ionics*, **179**, 742 (2008).

90. T. R. Jow, M. B. Marx and J. L. Allen, *J. Electrochem. Soc.*, **159**, A604 (2012).

91. T. Doi, Y. Iriyama, T. Abe and Z. Ogumi, *J. Electrochem. Soc.*, **152**,

A1521 (2005).

92. T. Abe, H. Fukuda, Y. Iriyama and Z. Ogumi, *J. Electrochem. Soc.*, **151**, A1120 (2004).

93. K. Xu, Y. Lam, S. S. Zhang, T. R. Jow and T. B. Curtis, *The Journal of Physical Chemistry C*, **111**, 7411 (2007).

94. S. Jurng, H.-s. Kim, J. G. Lee, J. H. Ryu and S. M. Oh, *J. Electrochem. Soc.*, **163**, A223 (2016).

95. C. Siret, C. Teissier, F. Castaing and P. Biensan, Lithium battery operating at very low temperature, in *SAFT Patents* (2010).

국문초록

리튬 이온 전지용 흑연 음극에서 황을 포함하는 첨가물의 표면 필름 형성 과정 및 저온 성능

정 선 형

서울대학교 대학원

화학생물공학부

리튬 이온 전지는 높은 에너지 밀도와 장기 수명특성을 가지고 있어 현재 휴대용 기기에 가장 많이 적용되는 에너지 저장 수단이며, 최근에는 하이브리드 전기자동차나 순수 전기자동차에도 그 적용범위가 확대되고 있다. 그러나 리튬 이온 전지를 이러한 운송 분야에 적용하기 위해서는 낮은 온도에서 급격한 성능 하락을 보이는 것을 포함하여 몇 가지 기술적인 문제가 해결되어야 한다. 특히 많이 사용되는 음극재인 흑연이 저온에서 좋지 않은 성능을 보이는 것이 잘 알려져 있다.

흑연 음극의 여러 가지 성능, 즉 비가역 용량이나 속도 특성, 수명특성, 안전성 등은 흑연의 표면에 형성된 부동태막(solid electrolyte interphase)의 특성에 영향을 받는다. 이 부동태막은 유기 전해질의 전기화학적 전위창이 흑연의 반응 전압보다 높기 때문에 구동 과정 중에 불가피하게 형성된다. 필름형성 첨가제를 이용하여 부동태막의 화학적 조성이나 물리-화학적 특성을 조절하여 리튬 이온 전지의 성능을 향상시킬

수 있다. 본 연구에서는 전극첨가제로 이용할 수 있는 원소상태의 황과 전해질에 첨가하는 알릴 설파이드(allyl sulfide) 두 가지 종류의 첨가제를 이용하여 흑연의 저온 성능을 개선하였다. 특히 안정성 면에서 후자가 더 유리한 것으로 나타났다.

먼저, 원소상태의 황이 부동태막을 형성하는 과정과 그에 따른 저온 성능 개선 효과를 살펴보았다. 첫 번째 충전 과정에서, 황은 전기화학적으로 환원되어 구동전해질에 용해되는 리튬 폴리설파이드(Li_2S_8)를 형성한다. 구동전해질과 리튬 폴리설파이드의 반응에서 싸이오카보네이트(thiocarbonates) 유기물이 생성되며, 형성된 싸이오카보네이트는 흑연 음극의 표면에서 전기화학적으로 분해되어 황을 포함하는 부동태막을 형성한다. 원소상태의 황이 첨가되었을 때, 흑연 음극의 저온에서의 가역 용량이 향상되었으며, 리튬 전착 반응 역시 지연되는 것을 확인하였다. 특히 전지의 저항 중 전하 전달 저항이 크게 줄어드는 것이 관찰되었다. 이 같은 저온 성능 향상은 원소상태의 황이 형성한 부동태막의 두 가지 특성, 즉 황 가교(sulfur bridge)로 연결된 고분자 구조와 저항의 요소로 작용할 수 있는 무기물 성분의 감소에 기인하는 것으로 생각된다.

두 번째로, 알릴 설파이드 전해질 첨가제에 대하여 같은 방식의 실험을 진행하였다. 알릴 설파이드 전해질 첨가제는 처음 전지를 조립한 후에 12시간 동안 진행하는 휴지기(rest period) 과정에서 자발적으로 흑연의 표면에서 산화되어 초기 피막을 형성한다. 이 피막은 충방전 과정을 거쳐 부동태막의 내부 피막으로 발달한다. 알릴 설파이드 역시 원소상태

의 황과 마찬가지고 흑연 음극의 저온 성능을 향상시키며, 전하 전달 저항을 감소시키는 효과를 보였다.

키워드: 저온 성능, 흑연, 황, 알릴 설파이드, 리튬 이온 전지

학 번: 2009-23957